Response Improvement of the PandaRoot Calorimeter Model

Bachelorarbeit
im Fachgebiet Experimentalphysik

vorgelegt von

Maximilian Rouven Rokuss
aus Frankfurt am Main

Prof. Dr. Kai-Thomas Brinkmann
II. Physikalisches Institut
Justus-Liebig-Universität Gießen

Gießen 2019

Contents

Zusammenfassung

Das $\overline{\text{P}}$ANDA-Experiment an der sich im Bau befindenden FAIR-Anlage wird eine der maßgeblichen Möglichkeiten sein, um tiefere Einblicke in die aktuellen Fragen der Teilchenphysik zu gewinnen. Es werden zum Beispiel Kollisionen zwischen Antiprotonen und festen Protonen- oder Kernzielen untersucht, um das "Confinement" von Quarks basierend auf der Theorie der starken Kernkraft zu verstehen und den Ursprung der Hadronenmassen zu untersuchen. Um Experimente am $\overline{\text{P}}$ANDA-Detektor im Vorfeld zu simulieren und zu analysieren, wurde das PandaRoot-Framework, das auf dem teilchenphysikalischen Datenanalyseframework ROOT basiert, etabliert. Neben Machbarkeitsstudien wird es später ein wichtiges Werkzeug für die Effizienzbestimmung zur Berechnung von Wirkungsquerschnitten sein.

Diese Arbeit konzentriert sich hauptsächlich auf die Optimierung des Ansprechverhaltens des elektromagnetischen Kalorimetermodells im PandaRoot Framework. Die Energieauflösung wurde analysiert und optimiert im Hinblick auf die experimentell abgeleitete Auflösungskurve. Die durchgeführten Tests und Überlegungen zeigten, dass die ursprüngliche PandaRoot Simulation zu falschen Ergebnissen führt, bei denen die Auflösung konstant besser ist, als diejenige, die bei Experimenten mit Prototypen ermittelt wurde. Daraufhin wurde die implementierte Berechnung der Auflösung weiter untersucht und mehrere Ansätze zur Korrektur der Auflösung diskutiert. Dies führte zu Überlegungen bezüglich des Berechnungsalgorithmus, die schließlich zu einem alternativen Modell zur Digitalisierung der im Kalorimeter erzeugten Treffer führten. Auf diesem neuen Weg wird die Auflösung vom Benutzer einfach durch die drei Koeffizienten der Response-Funktion definiert und kann leicht angepasst werden, was die Adaptierung an mögliche Ergebnisse zukünftiger Experimente erleichtert. Das neue Modell wurde erfolgreich mit den aktuellen Daten des jüngsten Prototyps PROTO120 getestet. Schließlich wurden viele Bugs und Mängel des bestehenden PandaRoot-Codes beobachtet, von denen einige behoben und andere untersucht werden konnten.

Abstract

The $\overline{\text{P}}$ANDA experiment at the currently built FAIR facility will be one of the key methods to gain deeper insights into the prevailing questions in particle physics. It will study for example collisions between anti-protons and fixed proton or nuclear targets to comprehend the confinement of quarks based on the theory of the strong force and investigate the origin of the hadron masses. In order to simulate and analyse experiments at the $\overline{\text{P}}$ANDA detector in advance, the PandaRoot framework, which is based on the particle physics data analysis framework ROOT, has been established. Besides feasibility studies, it will later be an important tool for efficiency determinations to calculate cross sections.

This thesis focuses mainly on the response optimisation of the electromagnetic calorimeter model in the PandaRoot framework. The energy resolution was analysed and optimised in regard to the experimentally deduced response function, which produced a variety of outcomes. The performed tests and considerations showed that the original PandaRoot simulation leads to wrong results where the resolution is constantly better than the response which was obtained from experiments with prototypes. Subsequently, the implemented calculation of the resolution was further investigated and several approaches to correct the resolution are being discussed. This led to re-considerations of the calculation algorithm ultimately resulting in an alternative model for digitising the hits which are generated in the calorimeter. Using this new path the resolution is defined by the user simply through the three coefficients of the response function and can be easily adapted as a possible cause of future experiments. The new model was tested successfully with the recent barrel prototype PROTO120 data. Lastly, many bugs and flaws of the existing PandaRoot code were observed of which some could be fixed and others were started to be investigated.

Chapter 1

Motivation and Introduction

"Nothing exists except atoms and empty space; everything else is opinion"
- Democritus, Greek philosopher

Looking back at the age of the ancient Greeks, there has always been the question of the smallest possible particles. Already around 400 BC the famous Greek philosopher *Democritus* proposed that the whole universe is composed of atoms in a void, which are constantly moving around according to determinate, understandable laws. [1] Since then, this question has further fascinated mankind.
Due to intensive research and newly developed technical possibilities there has been an immense leap in our scientific understanding of Elementary Particle Physics especially in the last century. Scientists are conducting research on the fundamental building blocks of nature which are governed by the forces between them. This experimental, but also theoretical work, ultimately leads to the so called Standard Model which has since been repeatedly confirmed by several experiments and discoveries. Most recently in 2012 the ATLAS [1] experiment at the European Center for Nuclear and Particle Research *(Conseil européen pour la recherche nucléaire)* (CERN) has detected a potential candidate for the Higgs boson which is a fundamental particle predicted by the Standard Model. [2]
In order to gain deeper insights into the Standard Model and our understanding of nature the "GSI Helmholtzzentrum für Schwerionenforschung" located in Darmstadt is currently being rebuilt into the Facility for Antiproton and Ion Research (FAIR). This new extension will provide new accelerators and detectors while using the existing GSI accelerators as the first acceleration stage. Scientists will have the possibility to simulate conditions that usually only exist in the depth of space and thus conclude on the evolution of the universe from the Big Bang to the present. [3] This thesis particularly focuses on the $\overline{\mathrm{P}}$ANDA[2] detector which is one of the four pillars at FAIR.
The $\overline{\mathrm{P}}$ANDA experiment aims on the production and detection of new particles enabled by the collision of protons (p) and anti-protons ($\overline{\mathrm{p}}$) with a beam energy between 1.5 GeV and

[1] A Toroidal LHC ApparatuS (ATLAS)
[2] Antiproton Annihilation at Darmstadt (PANDA)

$15\ \mathrm{GeV}$. The ultimate goal will be to gain deeper insights into the strong force (quantum chromodynamics), contributing to the search for glueballs and the question about the origin of the mass of matter.
In order to simulate the $\overline{\mathrm{P}}$ANDA detector in advance a team of scientists and code developers has been working on a framework which emulates the detector and possible experiments. This development ultimately resulted in the software package PandaRoot which is based on the Root framework originally developed by CERN. The program can simulate, reconstruct and analyse all kinds of possible decays of different experiments which can be set up by the user. The package also provides a variety of tools reaching from various analysing algorithms up to a detailed event display. The PandaRoot team is collaborating internationally to constantly implement new features and align the simulated detector with the specifications in the technical design report or experimental data from prototypes which have been obtained so far. This thesis in particular focuses on the simulated electromagnetic calorimeter, respectively its energy resolution.

1.1 The Standard Model

The Standard Model is the basis of our understanding of the fundamental interactions in the universe on a quantum scale. Although it was already introduced in the early 1970s, it is the currently established theory of elementary particles and their interactions in the physical reality. These can be experienced by human senses, but also via experiments with the exception of gravity. Until today, it remains in perfect agreement with experiment. [4] The Standard Model proclaims that fundamental particles are split in two groups, the quarks and the leptons. However, these are subdivided into three generations sorted according to their mass and stability. Starting with the lightest but most stable quarks and leptons in generation one the particles get less stable and heavier in the following two generations. This is illustrated in fig. 1.1 which displays the mass, charge and spin of the individual particles. The quarks and leptons in the figure are fermions which means they have a spin of $1/2$. Furthermore, each particle has an appendant antiparticle which has the same mass but inverted parity and charge. The fundamental particles of the Standard Model can interact through four fundamental forces. These are the electromagnetic, the gravitational and the strong and weak nuclear force. However, the gravitational force is not part of the Standard Model since its hypothetical exchange boson, the *graviton*, has not yet been aligned with the observations from nature or other theories, like general relativity. [5] The corresponding exchange bosons for the other forces are the photon γ for the electromagnetic force, the gluon g for the strong nuclear force and the Z^0, $W^{\pm}$ bosons for the weak force.

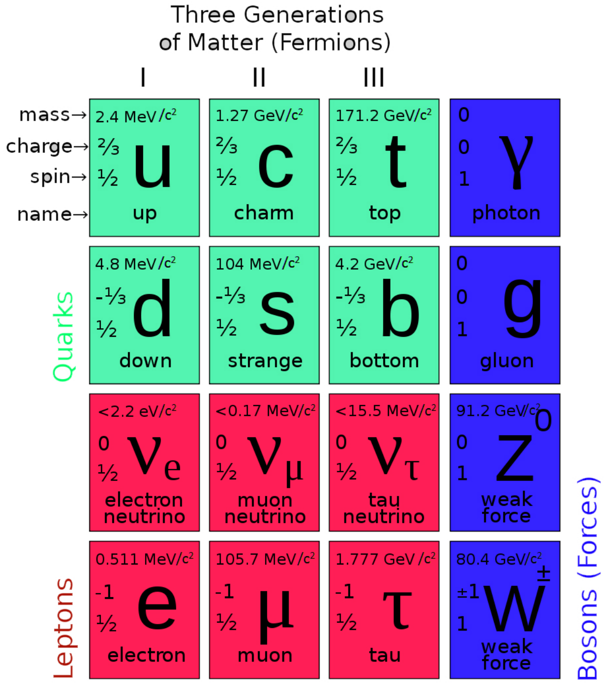

Figure 1.1: Overview of the different quarks (green) and leptons (red) given by the Standard Model. The exchange bosons of the four fundametal forces are marked in blue. [6]

It became clear that any further evolution in the field of particle physics will necessarily need to build on a precise understanding of the Standard Model. Thus several scientific institutions around the globe are conducting research with ever-increasing accelerators and detectors to study the smallest possible particles in our understanding. Usually every experiment has its own specifications aimed at a particular scientific outcome or area of interest. These experiments typically search for particles predicted by theory and offer hints about the interactions between different particles or even nuclei.
In an adapted form this happens at GSI [3] where they have the possibility to accelerate heavy ions ranging up to uranium. Recently the GSI company merged with FAIR to enter new fields of scientific research.

1.2 The FAIR facility

FAIR is an acronym for Facility for Antiproton and Ion Research and is an accelerator complex built as an extension of the GSI in Darmstadt. The goal is to study matter under extreme conditions to simulate an environment which is usually only found in space. This way scientists can gain a deeper insight in the composition of matter and the development of the universe. [3]

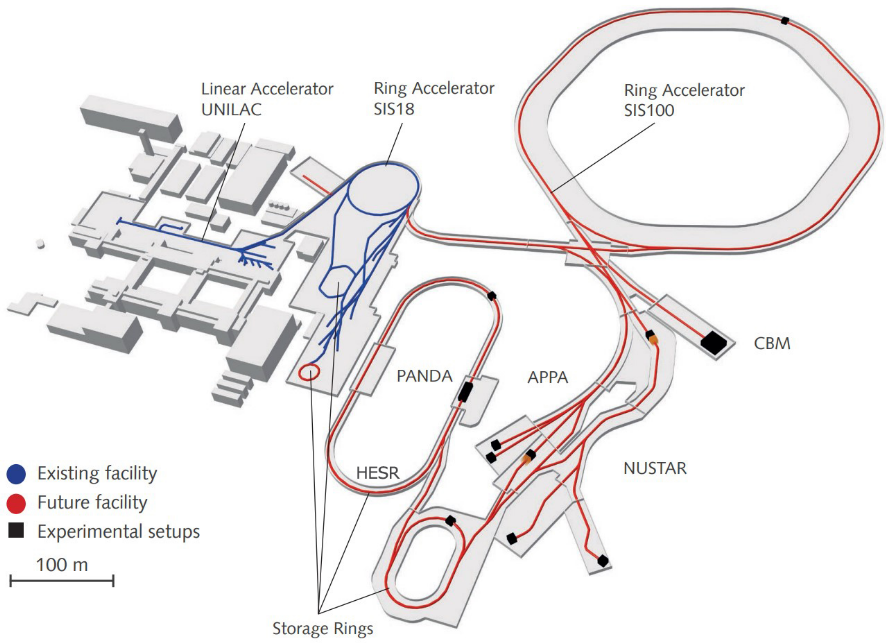

Figure 1.2: Schematic view of the existing GSI facility (blue) and the planned FAIR accelerators (red) in Darmstadt. [7] As shown the $\overline{\text{P}}$ANDA detector will be a part of the High Energy Storage Ring (HESR).

[3] Gesellschaft für Schwerionenforschung (GSI)

In order to be able to meet these high demands FAIR will provide an accelerator setup with a high luminosity and an extremely good beam quality. While the existing GSI linear accelerator UNILAC [4] and the SIS18 synchrotron will be used as the first acceleration stages, the new complex will provide a range of particle beams. These will reach from protons and anti-protons towards ion beams of all elements up to uranium combined with secondary beams of short-lived rare isotopes. The heart of acceleration and transportation of FAIR will be the superconducting double synchrotron SIS100 followed by a system of storage rings. [8] An areal view of the whole accelerator setup is shown in fig. 1.2.

The research at FAIR is divided into four main pillars: NUSTAR[5] is involved in experiments with atomic nuclei with the goal of a better understanding of stars. CBM[6] is investigating collisions of atomic nuclei at high speeds to temporarily simulate the conditions inside supermassive objects at nuclear densities, such as e.g. the formation of the quark gluon plasma. APPA[7] is about the investigation of atoms and macroscopic effects in materials or tissues extending to engineering and medical applications. Finally the goal of $\overline{\text{P}}$ANDA is to gain a better understanding of the mass of matter and the strong force using antimatter.

This thesis will focus on the $\overline{\text{P}}$ANDA experiment, which is placed at the High Energy Storage Ring shown in fig. 1.2. In the case of the $\overline{\text{P}}$ANDA detector, the antiprotons used for experiments are produced by the primary proton beam before they enter the ring. Inside the HESR they can collide with the fixed target inside the $\overline{\text{P}}$ANDA detector.

[4] Universal Linear Accelerator (UNILAC)
[5] Nuclear Structure Astrophysics and Reactions (NUSTAR)
[6] Compressed Baryonic Matter (CBM)
[7] Atomic, Plasma Physics and Applications (APPA)

Chapter 2

The $\overline{\text{P}}$ANDA experiment

The $\overline{\text{P}}$ANDA experiment, which is being built at the FAIR facility in Darmstadt, will study collisions between anti-protons and fixed proton or nuclear targets with a beam energy range from $1.5\ \text{GeV}$ up to $15\ \text{GeV}$. Using the cooled anti-protons from the HESR a peak luminosity of up to $2 \cdot 10^{32}\ \text{cm}^{-2}\text{s}^{-1}$ is envisaged. The resulting interactions can trigger a wide range of excited states and exotic hadronic systems. By investigating these interactions some of the main goals are to comprehend the confinement of quarks, based on the theory of the strong force and the origin of the hadron masses.

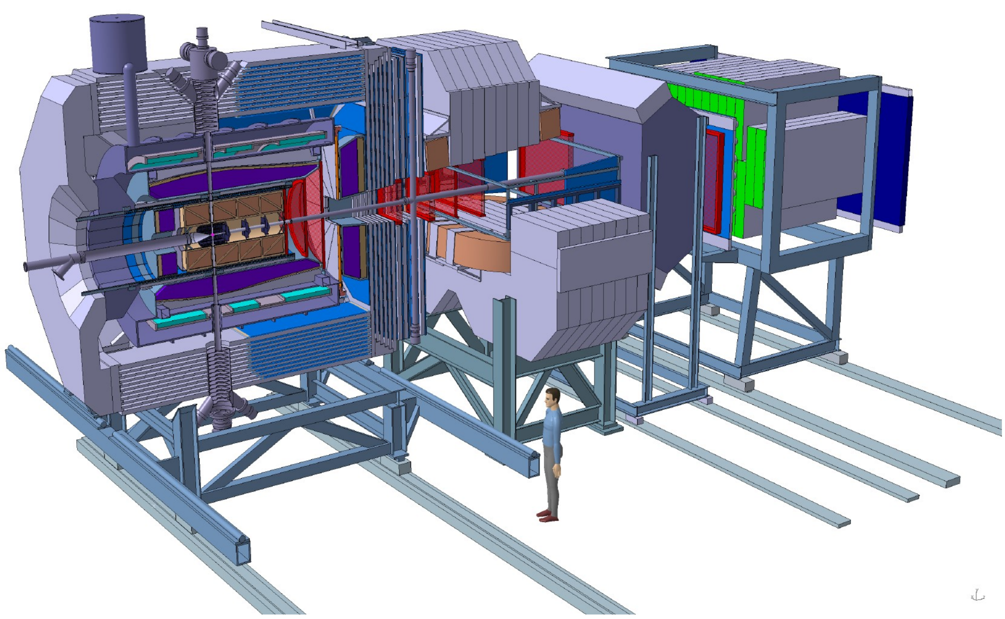

Figure 2.1: Schematic view of the $\overline{\text{P}}$ANDA detector with a human for scale. [9]

For this kind of experiment there are many requirements which have to be met by the detector to get the optimal setup for the reconstruction of the invariant mass, vertex and momentum. The most important issues designing the detector are a high resolution for tracking, particle identification and calorimetry, high rate capabilities, a versatile readout and event selection combined with a 99% 4π coverage.[9] A schematic visualisation of the planned detector is shown in fig. 2.1. The detector is split into a target spectrometer around the main interaction point and a forward spectrometer to separately analyse the forward-going particles. The interplay of these two subdetectors enables a complete angular coverage and is optimised for the wide range of energies.

To realise these demands the EMC[1] has to fulfil a variety of specifications reaching from a fast response time for high count rates up to the dynamic range of $10\ \mathrm{MeV}$ to $15\ \mathrm{GeV}$. In addition to that, the calorimeter must operate in a magnetic field of 2 T and has to be radiation hard and ultimately also compact to reduce cost. The University of Giessen is involved in designing and building the electromagnetic calorimeter and the MVD[2] of this detector.

2.1 The $\overline{\text{P}}$ANDA electromagenic calorimeter

As the detector itself the EMC is split into a homogeneous calorimeter in the target spectrometer and a sampling calorimeter which is used in the forward spectrometer. The different types of construction will be explained later, however, this division is made because in forward direction higher energies are to be expected. In the following the focus lies on the target spectrometer.

As outlined above, the EMC of the $\overline{\text{P}}$ANDA experiment has to meet several conditions given by the physics program. The homogeneous calorimeter will therefore consist of 15744 lead tungstate (PWO-II) crystals, which will be cooled to a temperature of $-25\ ^{\circ}\mathrm{C}$ to increase the light yield by factor 4 compared to room temperature. PWO-II is the second generation of lead tungstate ($PbWO_4$) which is a scintillator material especially developed for electromagnetic calorimetry. It has a relatively small radiation length of $X_0 = 0.89\ \mathrm{cm}$ combined with an scintillation decay constant of $\tau = 6.5\ \mathrm{ns}$. The second generation has an improved light yield while also being very radiation hard.

The desired threshold of 10 MeV for the photon reconstruction results in a threshold of 3 MeV per crystal.[9] A low threshold enables a more precise reconstruction since there is an increase in the detection of low-energy photons. This becomes especially vital when the detector is used for charmonium spectroscopy. Final state photons are then mainly produced through π^0 and η meson decays and have to be identified and distinguished from other photons which result from different decays. [10]
Apart from the division in forward and target spectrometer there is another subdivision of the target spectrometer calorimeter. It is split into three parts containing slightly different components optimised for the specific position. Fig. 2.2 visualises the components of the EMC with a picture taken from a PandaRoot simulation of the calorimeter.

[1] Electromagnetic Calorimeter (EMC)
[2] Micro Vertex Detector (MVD)

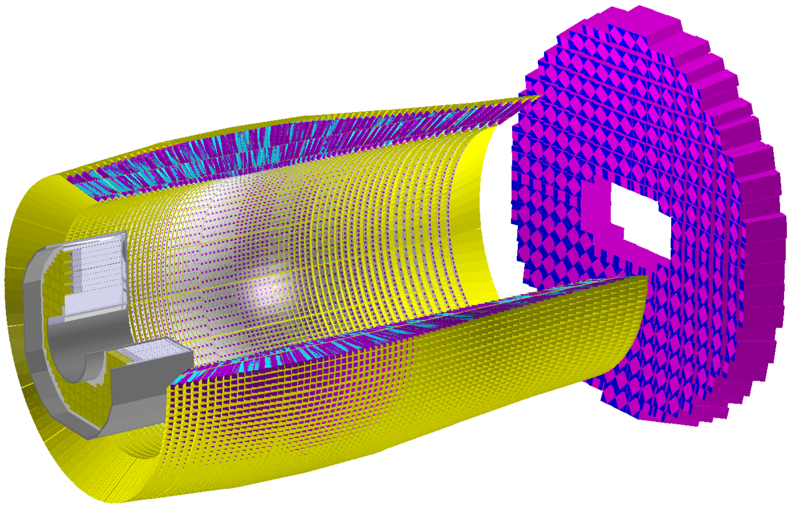

Figure 2.2: Clipped view of the $\overline{\text{P}}$ANDA target electromagnetic calorimeter simulated with PandaRoot. Shown are the backward endcap (left), the barrel (middle) and the forward endcap (right).

2.1.1 Barrel

The barrel is the main part of the target spectrometer EMC containing 11360 crystals. It covers the angular range from 22° to 140°. In contrast to both other components the barrel crystals are tapered which means they are not exactly cuboid but have a conical shape with the tip facing in the direction of the interaction point. To be more precise they are tilted by 4°next to the interaction point to minimise the effect of gaps or dead material. Apart from that the decisive difference between the components lies in the readout of the crystals with photodetectors. The magnetic filed of 2 T which engulfs the whole target spectrometer prevents the use of regular photomultiplier tubes. Another requirement is the radiation tolerance at an operating temperature of $-25\,^{\circ}\mathrm{C}$. Furthermore, the low threshold value of 10 MeV requires maximisation of the light yield.

At a foreseen barrel event rate between 10 kHz and 100 kHz the utilised photosensors were chosen to be adapted avalanche photo diodes[3]. These are basically the semiconductor equivalent to PMTs using the avalanche effect as an internal signal amplification. Combined with the high quantum efficiency of 70% this leads to the desired maximisation of the light yield. The utilised enlarged version is called Large Area Avalanche Photo Diode (LAAPD) with a surface coverage of $7 \times 13\ \mathrm{mm}^2$. Two of those are attached onto one crystal. Lastly the signal of the APDs are preamplified and shaped by an application specified integrated circuit[4]. This single chip is mounted on the backside of each crystal which which contributes to compactness of the EMC. It was especially developed for the $\overline{\text{P}}$ANDA calorimeter which gives it the acronym ASIC for PANDA Front-end Electronics (APFEL).

[3] Avalanche Photo Diode (APD)

[4] Application Specific Integrated Circuit (ASIC)

2.1.2 Forward Endcap

The forward endcap consists of 3864 PWO-II crystals. It covers the angular range from 5° to 22°. The angles below are covered by the sampling calorimeter in the forward spectrometer. In contrast to the barrel the crystals are only slightly tapered. Since the maximum expected annual radiation dose is expected to be 125 Gy in the forward endcap the readout components have to be especially radiation hard. This increased radiation combined with an expected event rate of 500 kHz also prevents the use of APDs. The utilised photosensors are vacuum photo tetrodes. These are basically PMTs with a reduced number of dynodes which in this case are two dynodes. This reduction is done to ensure the function in the magnetic field. Vacuum photo tetrodes are ideal for high event rates and very radiation hard. They have a quantum efficiency of $\eta > 15\%$.

2.1.3 Backward Endcap

The backward endcap is the smallest component of the target spectrometer EMC. It covers the angular range from 140° up to 180°. It consists of non-tapered crystals which are also read out with APDs since they have a higher gain and quantum efficiency than VPTs. Those are useful at the low energies expected in the backward region which allows efficient reduction of background. [9]

Chapter 3

Calorimetry and Theory

The term *calorimetry* generally refers to the act of measuring energy. In thermodynamics calorimetry is a method to determine the quantity of heat, whereas in particle physics it is a ubiquitous principle to measure the energy of (high energetic) particles. Initially invented to investigate cosmic-rays, this technique was developed and adapted for accelerator-based experiments measuring mostly the energy of photons, electrons and hadrons. It works by particles being completely absorbed in the calorimeter material. This means the detection of particles in calorimeters is eradicating them while their energy is transformed into a measurable quantity. If a particle hits the detector it can interact with the material in several ways which is discussed in section 3.1. In general this results in a shower of secondary particles which have a progressively degraded energy. By measuring the energy of all generated particles, usually detected in the form of charge or light, one can draw conclusions about the initial particle energy. [11] In particle physics calorimeters can generally be classified into one of two types. One the one hand, the electromagnetic calorimeter which is sensitive for electromagnetically interacting particles such as electrons and photons and on the other hand the hadronic calorimeter detecting hadrons via strong and electromagnetic interactions. This thesis focuses mainly on the EMC when speaking of calorimeters since the workgroup at the University of Giessen is involved in designing and assembling this particular component of the $\overline{\text{P}}$ANDA detector.

3.1 Interaction of particles with matter

When particles hit matter they generally interact with the constituents of the target, in fact with the atoms or more specifically with the electrons and nucleons. Typically two phenomena can occur: The initial particle can either be scattered or absorbed, which usually results in a loss of energy. The occurring effects are mainly dependant on the mass, energy and charge of the particle together with the distance between the centres. However, it is still possible that there is no interaction at all.
The interaction of particles with matter is a statistical process, since the fundamental effects are derived from quantum mechanics. This means that only a probability of the result can

be obtained, which is done through repeating many iterations of the same setup.[12] In the case of an EMC the interaction of photons with matter is of particular interest. The photon is a massless and neutral particle which interacts electromagnetically. It propagates as an electromagnetic wave with the speed of light while its energy is only dependant on the frequency respectively the wavelength.

$$E = h \cdot f = h \cdot \frac{c}{\lambda} \tag{3.1}$$

Generally if a photon interacts with matter three effects prevail, each dominant at a different energy range.
At low photon energies starting at 5 eV and reaching up to a few hundred keV the photoelectric effect can occur. This effect describes the emission of an electron which has been knocked out of its bond by the photon. The photon is absorbed by the bound electron resulting in the initial energy being transferred onto the electron. The electron is ejected if the photon energy is higher than the electron binding energy in the material. Its energy can be described as in eq. 3.2 where f is the frequency of the impinging photon and ϕ the workfunction of the material.

$$E_{kin} = hf - \phi \tag{3.2}$$

At energies between 50 keV and 1 MeV the compton effect is of relevance. This phenomenon is an alteration of the wavelength and direction of a photon due to the scattering at an electron. To be more precise an elastic scattering takes place at a virtually free electron where a part of the energy is transferred from the photon onto the electron. This results in the wavelength of the scattered photon being longer than the initial wavelength and a scattering angle θ of up to 180°. The relation between the deflected angle and and the resulting difference in wavelength can be described as shown.

$$\Delta\lambda = \frac{h}{m_e c}(1 - \cos\theta) = \lambda_c(1 - \cos\theta) \tag{3.3}$$

In this equation m_e is the electron mass and λ_c is commonly known as the *compton wavelength*. The energy which is passed onto the electron is then given by

$$\Delta E_e = E_\gamma - E_{\gamma'} = E_\gamma \left(1 - \frac{1}{1 + \frac{E_\gamma}{m_e c^2}(1 - \cos\theta)}\right) \tag{3.4}$$

If a photon crosses the energy of 1.022 MeV pair production is possible and becoming the dominant effect with increasing energy. This effect describes the electron-positron pair generation from a high-energy photon near the nucleus. Due to conservation of energy the phenomenon has the threshold of 1.022 MeV since this is twice the rest energy of an electron. In addition to that, conservation of momentum prevents this effect from happening in a vacuum so the electromagnetic field of a nucleus is needed so that the momentum can be absorbed. The kinetic energy which is transferred onto the electron positron pair is described by

$$E_{kin} = hf - 2m_e c^2 \tag{3.5}$$

Finally the absorption of photons in a sample material with the corresponding effects is displayed in fig. 3.1. In this case the graph is shown for lead since this is a component of the scintillator material used in the $\overline{\text{P}}$ANDA EMC.

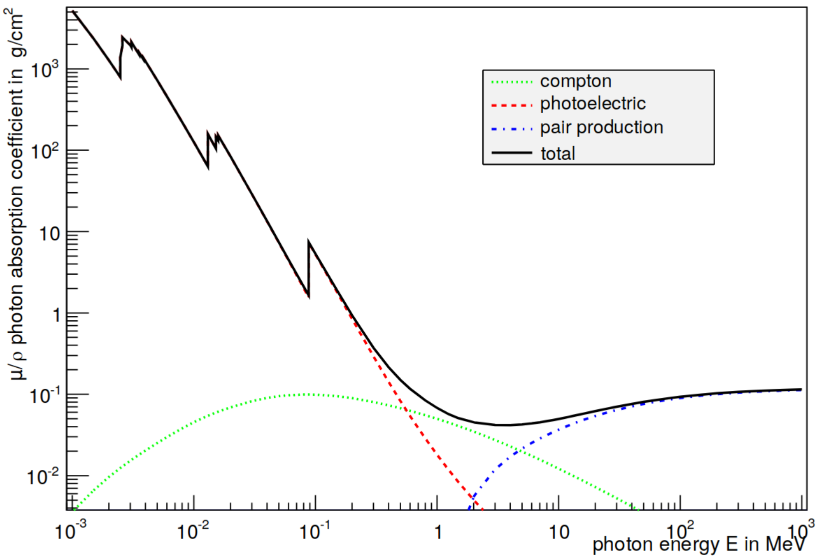

Figure 3.1: The photon absorption coefficient μ/ρ for a sample material (here: lead) plotted against the photon energy. [12]

The described effects lead to a decrease in intensity when photons pass through matter. This loss of intensity can be described by the law of Beer-Lambert.

$$I(x) = I_0 e^{-\mu x} = I_0 e^{(\tau+\eta+\kappa)x} \tag{3.6}$$

In this equation the coefficients τ,η and κ illustrate the composition of the attenuation coefficient μ from the different influences of the photoelectric effect, compton scattering and pair production.

In a calorimeter the incident particle produces many secondary particles as explained in the following sections. Those secondary particles can be charged so it is of great interest to describe the interaction of charged particles with matter as well. Furthermore, an electromagnetic calorimeter is also used for detecting charged incident particles. Those can lose their energy when traversing through matter generally via five different effects.

1. Ionisation
2. Excitation
3. Bremsstrahlung
4. Cherenkov radiation
5. Transition radiation

In an electromagnetic calorimeter those particles typically lose their energy in matter mainly through bremsstrahlung and ionisation. The process of ionisation is well described by the Bethe-Bloch formula in eq. 3.7.

$$-\frac{\mathrm{d}E}{\mathrm{d}x} = \frac{4\pi}{m_e c^2}\frac{nz^2}{\beta^2}\left(\frac{e^2}{4\pi\epsilon_0}\right)^2\left[\ln\frac{2m_e c^2\beta^2}{I(1-\beta^2)} - \beta^2\right] \tag{3.7}$$

with z as the particle charge, n the electron density of the target, I the mean excitation potential of the target and the relativistic coefficient $\beta = v/c$. The characteristic shape of this curve is shown in fig. 3.2. By plotting the energy loss per unit depth against the momentum or kinetic energy it is possible to determine the observed particle on the basis of this particular shape and position. It has to be noted that the energy loss is hereby only dependant on the charge and velocity of the impinging particle.

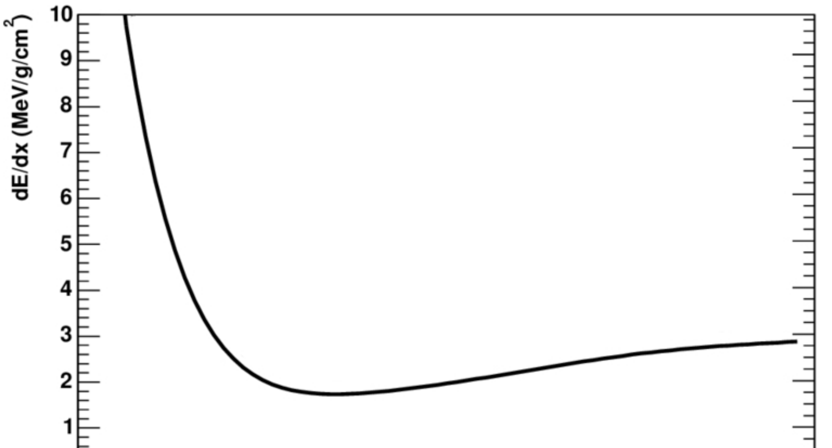

Figure 3.2: The energy loss per unit thickness of an electron in air as a function of its kinetic energy. [13]

However, at high energies charged particles lose their energy via bremsstrahlung. This effect is based on the deflection and therefore acceleration of the impinging particle by the coulomb field of the absorber. It is the dominant effect at energies above the critical energy which is further explained in section 3.3 since it is a vital effect for calorimetry.

3.2 Structure of a calorimeter

Electromagnetic calorimeters employed in particle physics detectors can be generally subdivided into two groups. Homogeneous calorimeters and sampling (or shashlik) calorimeters. The first type consists of just one material performing the absorption of the particles together with the scintillation process to measure the energy based on the amount of light produced. In a sampling calorimeter those two processes are separated using two different materials repeatedly stacked after each other. The dense and passive absorption material is responsible for the effective stopping of the particles while the active scintillator material produces the quantifiable light which generates the signal. In general, a sampling calorimeter is used for measuring extremely high energetic particles since it has a higher stopping power but also a worse resolution. Figure 3.3 illustrates the two types. Typical examples are lead and copper as absorber and silicon or plastic as a scintillator material.

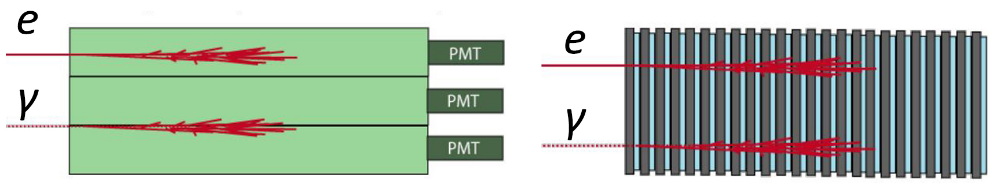

Figure 3.3: Schematic illustration of the two types of calorimeter designs with the homogenous calorimeter on the left an the sampling calorimeter on the right. [14]

Regardless of the different types they are both based on the same principles. If a detectable particle hits the calorimeter it interacts with its matter. Due to the dense material it is ideally fully stopped in the process of an electromagnetic shower which is further explained in the following section. The light produced by the shower in the scintillator is directly proportional to the initial particle energy. It is then typically read out with photomultiplier tubes (PMTs) or similar devices. These are instruments which are capable of detecting small quantities of light. The fundamental principle is the photoelectric effect where the incoming photons knock electrons from the photocathode out of their bond. After passing through a focusing electrode these are then accelerated by several dynodes. The dynodes are basically capacitor plates with increasing voltage so that the electrons are always accelerated between them. Simultaneously when colliding with the dynodes the electrons knock out other electrons so that their number multiplies with each dynode. This ultimately results in an avalanche effect with an amplification of up to 10^6 of the initial quantity. These are the electrons that produce the electrical pulse which is passed on to the further readout chain. Fig. 3.4 exemplifies this procedure.

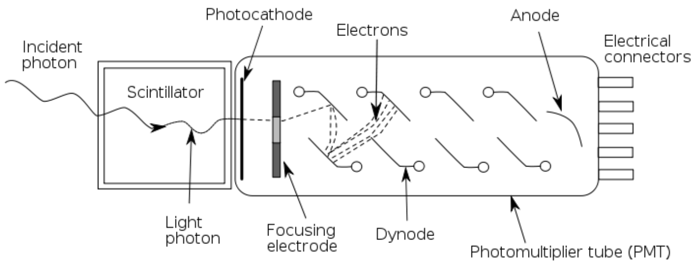

Figure 3.4: Schematic of a photomultiplier tube connected to a scintillator. [15]

In fact there are also other electrical components which are used instead of the PMTs such as the avalanche photo diode which works on the basis of a semiconductor. When a high reverse bias voltage is applied these photo diodes show an internal current gain which results of the impact ionisation and causes the so called avalanche effect. The avalanche electrons can then be detected as a pulse initially triggered by the impinging photon. Another type is the vacuum photo tetrode which is basically a PMT with less dynodes. It is typically utilised in strong magnetic fields where normal PMTs do not work. Despite the different kinds of photo diodes which are optimised for distinct environment variables they are all used to turn the emitted scintillation light into a measurable pulse.

3.3 Physics of the electromagnetic cascade

The light which is ultimately used to determine the energy of the initial particle is produced by an electromagnetic shower. These cascades are basically a sequence of pair production and bremsstrahlung processes.
If the incoming particle is a high energetic electron or positron it loses its energy while passing through matter mainly via bremsstrahlung. This process is the radiation of photons in the electric field of the atomic nucleus. The radiation is a result of the deceleration of the charged particle while being deflected by the nucleus. The loss of kinetic energy is directly transferred onto the photon to fulfil the law of conservation of energy. The energy loss per unit depth of electrons passing through matter can be described as: [16]

$$-\frac{dE}{dx} \approx \frac{E}{X_0} \tag{3.8}$$

$$\Rightarrow E(x) = E_0 \exp\left(-\frac{x}{X_0}\right) \tag{3.9}$$

where X_0 is the radiation length, which is a material-specific constant. It characterises the rate of loss in a material where the value describes the length at which the electron has only $1/e$ of its initial kinetic energy. The radiation length with respect to the partial screening of the nuclear change by the electrons can be expressed as: [16]

$$X_0 = \frac{716.4A}{Z(Z+1)\ln{(287/\sqrt{Z})}} \propto \frac{1}{Z^2} \tag{3.10}$$

In this case A is the atomic mass and Z the proton number. The radiation length of the utilised scintillation material in the $\overline{\text{P}}$ANDA calorimeter crystals is approximately $X_0(\text{PbWO}_4) \approx 0.89\ \text{cm}$.

Apart from that for high energetic photons the dominating process for interaction with matter is pair production. Thus pair production and bremsstrahlung processes are closely related since at high energies the photons emitted through bremsstrahlung can themselves result in a pair production and vice-versa. This sequence of events is called an electromagnetic shower because the energy of the impinging particle is spread across many secondary particles in a cascade process which looks like a shower. On average, the particles interact after one radiation length which results in a doubling of the number of particles. Accordingly the energy of each particle is decreasing with the number n of radiation lengths as shown in equation 3.11.

$$E(n) = \frac{E_0}{2^n} \tag{3.11}$$

A schematic view of the whole process is drawn in fig. 3.5 where an incoming photon starts an electromagnetic cascade.

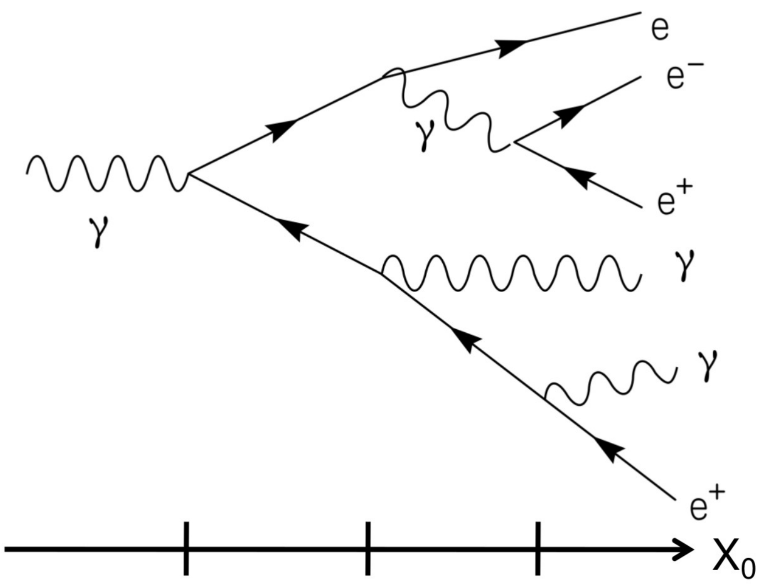

Figure 3.5: Schematic view of an electromagnetic shower where the amount of particles roughly doubles each radiation length. [17]

The shower is ultimately stopped when the electrons start to lose their energy through ionisation and excitation. The process of ionisation dominates over bremsstrahlung at lower energies than the critical energy E_c . The critical energy is defined as the energy for which the rates of loss through bremsstrahlung and ionisation are equal. An approximate expression for elements with $Z > 12$ is given by: [16]

$$E_c = \frac{550}{Z} \text{ MeV} \tag{3.12}$$

The critical energy of the $\overline{\text{P}}$ANDA calorimeter material is approximately $E_c(\text{PbWO}_4) \approx 9.5$ MeV [17]. The maximum number of particles is then given by:

$$N_{max} = \frac{E_0}{E_c} \tag{3.13}$$

The final particles at the end of the cascade are responsible for the detectable scintillator light. The amount of light is directly proportional to the energy of the impinging photon or electron. It remains to be noted that for lower energetic photons the Compton and photoelectric effect are of increased dominance as fig. 3.1 shows. However, the photons measured in particle physics typically have energies above the threshold of several MeV. Based on equation 3.9 the maximum depth of the occurring shower can be scaled as:

$$d_{max} = X_0[\ln\left(\frac{E_0}{E_c}\right) + \alpha] \tag{3.14}$$

The depth is dependant on the type of the incoming particle which is taken into account by the parameter α. For photons α equals $+0.5$ whereas for electrons $\alpha = -0.5$. Furthermore, the shower has a specific width which is primarily caused by the scattering of the electrons. This spread is described by the Molière radius in eq. 3.15 [16].

$$R_M = \frac{21 \text{ MeV}}{E_c} X_0 \tag{3.15}$$

In sufficient approximation a cylinder with the radius of R_M contains 90% of the shower energy. This observation is of great significance when designing the individual crystals used for calorimetry. The dimensions have to meet the ideal ratio between spatial resolution and shower containment.

3.4 Energy resolution of calorimeters

Per definition the resolution is a measure of the sharpness of a peak. It is of great importance e.g. when two peaks occur relatively close to each other because an increased resolution enables a better separation of the individual peaks. The definition of the resolution relies on the peaks width which is commonly described by the FWHM[1]. This is the distance between the two points of the curve which lay at half the height of the peak itself. In most

[1] Full Width at Half Maximum (FWHM)

cases the arising peaks can be described with a Gaussian distribution where the FWHM is connected to the standard deviation σ as shown in eq. 3.16.

$$\sigma = \frac{\mathrm{FWHM}}{2\sqrt{2\ln 2}} \tag{3.16}$$

Especially in the field of calorimetry the relative resolution is prevalently used. This parameter gives the relation between the width of a peak and its position (usually the mean). This way the resolution is dependant on the energy which results in the possibility to obtain an energy resolution curve where the relative resolution is plotted against the measured energy. The relative resolution is a dimensionless number which is usually expressed as a percentage.[12] It is an important factor in calorimetry because it describes the statistical uncertainty of a single measurement. This section will derive a theoretical description of the energy resolution formula used for particle physics calorimeters.

As explained in the last section it is clear that the electromagnetic cascade is a stochastic process. The shower results in the production of n secondary particles in total, where the mean value of n is proportional to the initial energy:

$$\langle n \rangle \propto E_0 \tag{3.17}$$

However the amount of secondary particles produced is subject to fluctuations. These are a major factor influencing the energy resolution by means of $\sqrt{n}$. Combined with eq. 3.17 the following relationship applies for the energy dependence of the resolution:

$$\left(\frac{\sigma}{E_0}\right) \propto \frac{1}{\sqrt{n}} \propto \frac{1}{\sqrt{E_0}} \tag{3.18}$$

This dependency is called the intrinsic energy resolution as it accounts for the fluctuations of n governed by Poisson statistics. Due to the variety of components and their imperfections each calorimeter also has other parameters contributing to the resolution. Thus, the resolution is further dependant on the measured energy and can generally be divided into three terms as shown in equation 3.19.

$$\left(\frac{\sigma}{E}\right) = \sqrt{\left(\frac{a}{\sqrt{E}}\right)^2 + \left(\frac{b}{E}\right)^2 + c^2} =: \frac{a}{\sqrt{E}} \oplus \frac{b}{E} \oplus c \tag{3.19}$$

The first term with the coefficient a was already discussed and is called the *stochastic term*. It describes the fluctuation in the amount of detected photoelectrons n_{pe} which is also called the light yield LY. The coefficient a can approximately be expressed by combining the "Fano factor" F with n_{pe} as in eq. 3.20 [16].

$$a = \sqrt{\frac{F}{n_{pe}}} \tag{3.20}$$

The factor F takes into account that the energy loss in a collision is not purely statistical and furthermore ionising an atom is restricted to the discrete electron shells. The Fano factor or "Excess Noise factor" becomes especially vital when using avalanche photodiodes as for example in the $\overline{\text{P}}$ANDA calorimeter. This is because APDs generate excess noise as a result of the statistical nature of the avalanche process. F is the factor by which the statistical noise on the APD current exceeds the value which would be expected from a noiseless multiplier on the basis of Poisson statistics (shot noise) alone. It can be calculated as in eq. REF. [18]

$$F(M) = kM + (1-k)\left(2 - \frac{1}{M}\right) \tag{3.21}$$

In this expression M is the gain and k is the carrier ionisation ratio which is defined as the ratio of hole to electron ionisation probabilities.

The second term in eq. 3.19 indicated by the coefficient b is generally referred to as the *noise term*. It is used to describe the noise generated in the readout electronics. Furthermore, it takes other effects into account such as "pile-up" which is the simultaneous detection of uncorrelated particles.

The third term with the coefficient c is called the *constant term*. Many factors in a calorimeter affect the resolution regardless of the energy. These are typically dependant on the particular design and can be the energy loss in dead material, non-uniformities in signal collection, channel-to-channel calibration errors or imperfections and tolerances in the construction. [18] Also the tapering of crystals plays a role which is an important issue in the $\overline{\text{P}}$ANDA calorimeter. As eq. 3.19 shows the relative resolution improves with increasing energy because E is in both cases below the fraction line. However, the constant term limits this descent. Generally the goal in designing a calorimeter is to find the best compromise between all three terms to achieve the optimal resolution on the desired energy spectrum.

3.5 Novosibirsk function

The Novosibirsk Fit (later referred to as "Novo-Fit") is a method to align a Gaussian like function onto bell curves with a one-sided tail. It uses the Novosibirsk function [19] which is an altered Gaussian as shown in eq. 3.22. The function basically describes a non-symmetrical Gaussian with a tail on one side.

$$f(A, \Lambda, x_0, \tau) = A \cdot e^{-\frac{1}{2}\cdot\left(\ln^2(\tau)/\Lambda^2 + \Lambda^2\right)} \tag{3.22}$$

with

$$\tau = 1 + \frac{\Lambda(x - x_0)}{\sigma} \cdot \frac{\sinh(\Lambda\sqrt{\ln 4})}{\Lambda\sqrt{\ln 4}} \tag{3.23}$$

where A is the amplitude, x_0 is the peak position, Λ represents a parameter describing the tail of the distribution and σ is the width of the peak which can also be expressed via the FWHM according to formula 3.16.

In the case of calorimetry this method can be extremely useful. To reconstruct the total photon energy E the deposited energy in the crystals E_i is accumulated as shown.

$$E = \sum_i E_i$$

Due to an insufficient deposition of the photon energy, it is expected that the energy spectra do not have a symmetrical Gaussian shape. Possible causes are that part of the energy is scattered from the active volume or absorbed in the dead material between the crystals. Since the barrel is composed of several slices and modules there are different dead spaces between calorimeter elements which are shown in fig. 3.6.

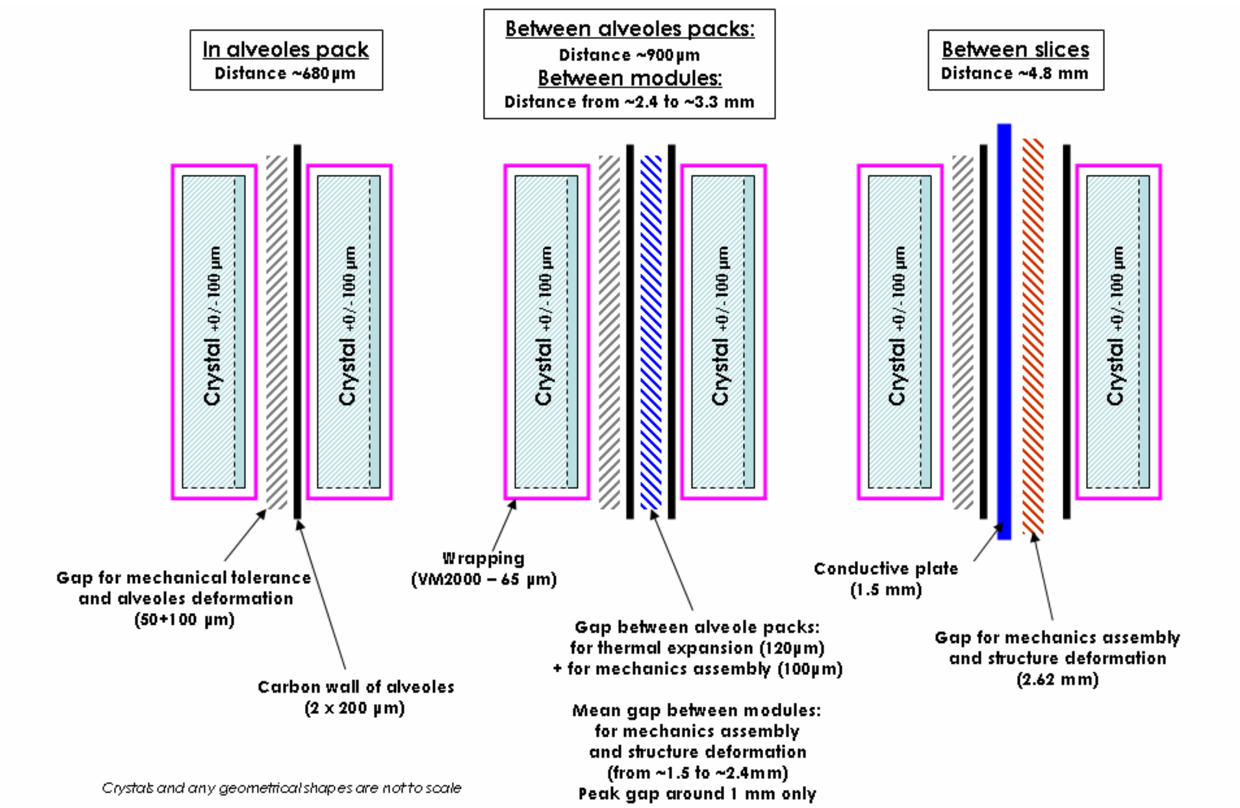

Figure 3.6: Schematic view of the foreseen dead material between the crystals. [9]

The resulting energy peaks can be parameterised by the Novosibirsk function. [20] The energy resolution is then obtained by plotting the photon energy spectrum. Near the incoming energy value the photon hits accumulate to a peak. The resolution is then defined as the width of the peak divided by the peak position. Thus it can be calculated using the width and peak of the fit while the error originates from the propagation of uncertainty as shown below. The errors of the fitting parameters are given by the fit macro.

$$\left(\frac{\sigma}{E}\right) = \frac{\sigma_{\text{fit}}}{x_0} \tag{3.24}$$

$$\Delta\left(\frac{\sigma}{E}\right) = \sqrt{\left(\frac{1}{x_0}\Delta\sigma_{\text{fit}}\right)^2 + \left(-\frac{\sigma_{\text{fit}}}{x_0^2}\Delta x_0\right)^2} \tag{3.25}$$

The expressions above are used throughout the thesis to calculate the energy resolution and the corresponding error from simulated histograms.

Chapter 4

PandaRoot

In order to simulate and analyse experiments at the $\overline{\mathrm{P}}$ANDA detector in advance the PandaRoot framework has been established. Based on the particle physics data analysis framework ROOT which was originally developed by CERN, PandaRoot is an extension especially adapted for the $\overline{\mathrm{P}}$ANDA detector.

ROOT is an object oriented large scale data analysis framework. It is coded in C++ and also contains a C++ interpreter. ROOT enables advanced statistical analysis like multi-dimensional histograms, fitting and minimization and has integrated cluster finding algorithms and visualisation tools. The user interacts with ROOT via a graphical user interface, the command line or batch scripts. [21] Nowadays ROOT is a general standard program in many particle physics experiments and simulations.

This ROOT system was used as a foundation for the PandaRoot framework. PandaRoot is part of the FairRoot project which is a general software package for simulations and future experiments at FAIR. It is used to simulate the performance of the detectors as well as reconstruction and data analysis and served to evaluate different detector concepts. [22] The simulations are made possible by GEANT3 and GEANT4 together with virtual Monte Carlo. GEANT [1] is a toolkit suited for simulating the passage of particles through matter, whereas virtual Monte Carlo represents a ROOT implementation of Monte Carlo simulations.

To provide a unified package and obtain a standardised computing structure for future FAIR experiments (eg. PANDA, CBM and APPA) PandaRoot is based on FairRoot as shown in fig. 4.1. FairRoot is an object oriented simulation, reconstruction and data analysis framework. It takes care of the basic features, such as the interfaces with simulation, geometry handling, offline analysis of particle physics data and the parameter database. The software provides the user with a unified way to design and construct their detectors or analysis tasks, while it also delivers some general functionality like track visualisation. [22][23] The whole framework also provides a detailed event display which can be used to

[1] Geometry and Tracking (GEANT)

view the detector and the respective events in three-dimensional space.
When the detector is operating in the future, PandaRoot will be used to evaluate results, for example to estimate efficiencies. The readout chain after the digitisation will be virtually the same and also the analysis agorithms are important tools to interpret the experiments. This shows that it is especially vital to trim the software framework PandaRoot to the optimal alignment with current experimental data and ultimately the whole detector, since the results of simulation and experiment can later be compared this way.

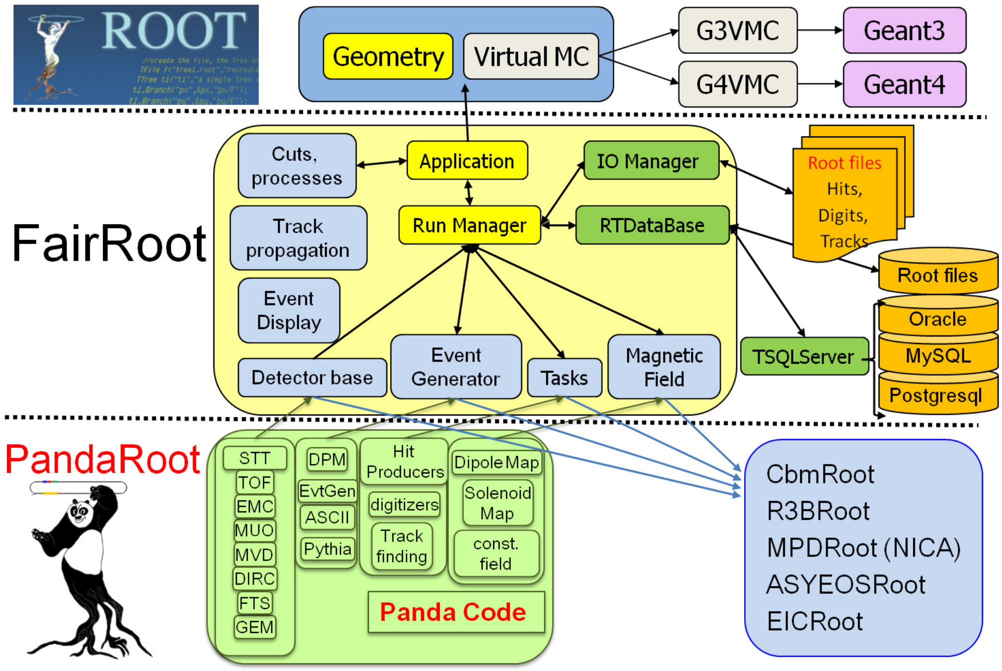

Figure 4.1: Schematic of the PandaRoot Framework. The top level contains ROOT and virtual Monte Carlo. The middle layer manages the general infrastructure with simulation and other tasks enclosed by the FairRoot framework. Detector details and reconstruction are being managed at the bottom level. [24]

4.1 PandaRoot EMC data flow

In order to improve the conformity of the simulated $\overline{\text{P}}$ANDA electromagnetic calorimeter compared to the real detector it is crucial to get an overview of the readout chain.

After the simulation which is performed by GEANT with the predefined geometry data each event is processed by the PandaRoot code. This process is generally divided into three major parts. The simulation creates `EmcPoints` in the crystals where a shower is created. All of these points in one single crystal are then accumulated to `PndHits`. These hits are then passed on to the digitisation. In PandaRoot there are two ways implemented to digitise the events as shown in fig. 4.2.

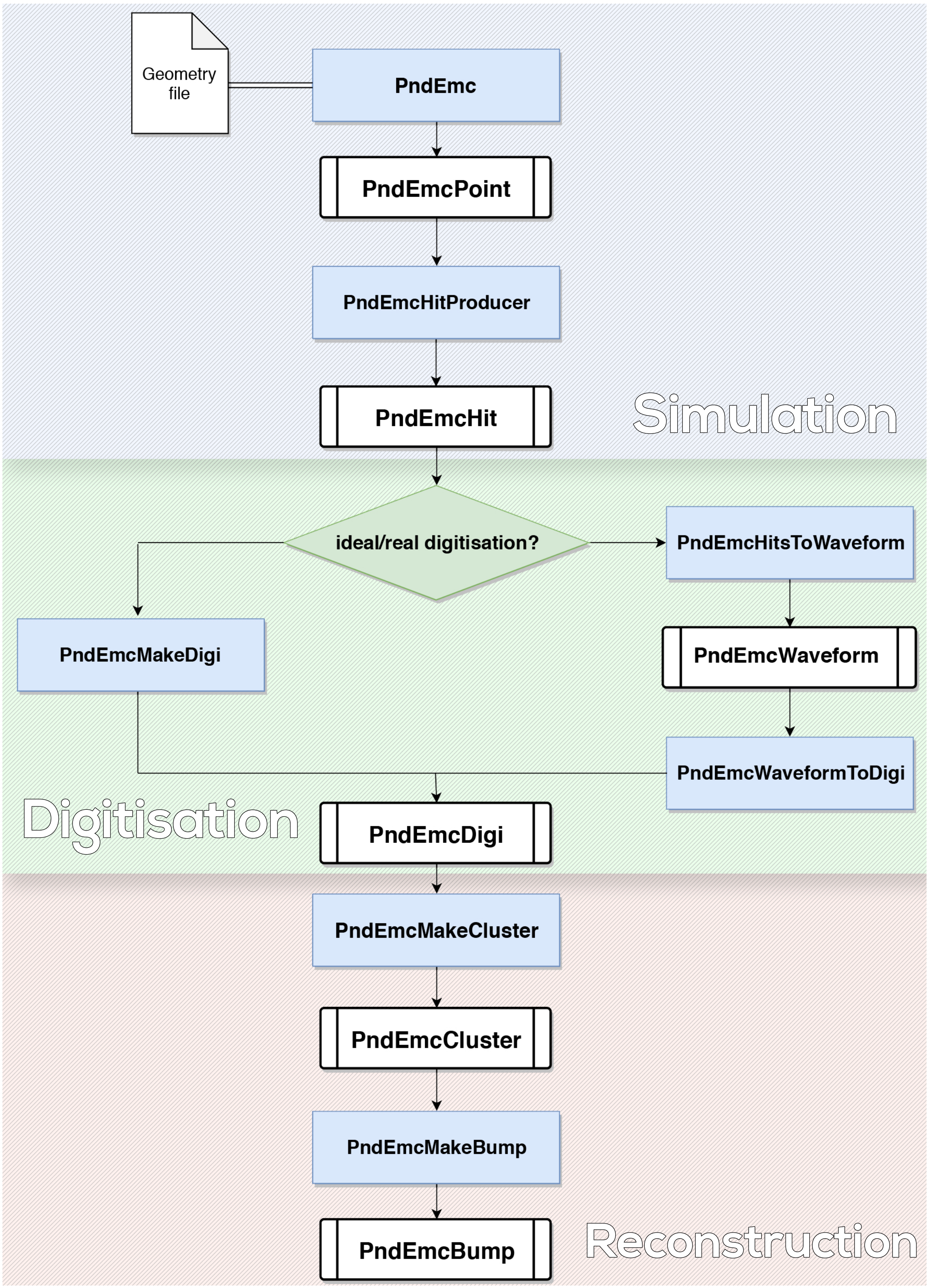

Figure 4.2: Data flow of the PandaRoot electromagnetic calorimeter starting with the simulation over the digitisation up to the reconstruction. The blue boxes represent functions while the white shapes are different classes in the process.

The default method is the so called real digitisation. The program creates `PndEmcWaveforms` out of the hits which are then being digitised. This is especially beneficial for time-based simulations when two hits occur in rapid succession. The other way is to directly digitise the hits. It is called the ideal digitisation and is a more simple and transparent approach. It offers the opportunity to change the parameters needed for digitising more easily and will later be used to align the simulated data with the experiment. Ultimately both ways produce a `PndEmcDigi` which will be used in the further data flow.

After digitisation the reconstruction phase begins where the digitised hits are combined to clusters and bumps. A `PndEmcCluster` is formed out of several digitised hits if the angular distances of the particles are small. Then `PndEmcBumps` are created at local maxima inside the clusters where all neighbouring energy values are smaller.

The collaboration has worked on different reconstruction algorithms in order to improve the significance and reduce the background. The last step in the readout chain is the particle identification (PID), which uses the digitised clusters and bumps to create possible particle candidates.

4.2 PandaRoot data analysis

The analysis of simulated and reconstructed data is also based on the original framework Root. At the front end plots and fits are done by Root whereas PandaRoot provides analysis algorithms optimised for various decay channels and the detector layout. The user has the possibility to chose from different algorithms to obtain a global PID probability, where one can select the preferred particle list. Furthermore the Rho package has been included to combine hits, fit with constraints, apply cuts and ultimately retrieve the MonteCarlo truth match. Various kinematic and vertex fitters have also been implemented.[24] Currently several groups are working on optimised algorithms for better event reconstruction and reduced background.

Chapter 5

Energy Resolution of PandaRoot

As explained earlier PandaRoot is a framework for simulation, reconstruction and data analysis based on ROOT, which was especially adapted for the $\overline{\text{P}}$ANDA detector. When using this software for reconstruction and data analysis it is especially vital that the photon energy and its resolution are simulated correctly according to how the real detector would behave. Photons are particularly important because many decay channels ultimately produce photons of several different energy values which can be measured by the detector. Furthermore, by obtaining the correct decay width of a particle via resonance scan utilising the accelerator its mean lifetime can be calculated which shows that not only the position of the peak but also the width is an important value in particle physics. In this case a precise allocation of final stage photons to the resonance of interest is very important. This shows that precisely measuring the photon energies contributes in a major way to the reconstruction results.
This is the reason why an investigation of the default PandaRoot EMC resolution was started. After determining the original response curve it turned out that it did not match with the experimental data. This led to re-considerations of the calculation algorithm ultimately resulting in an alternative way of digitising the hits.

5.1 Energy resolution of default PandaRoot

To determine the energy resolution of PandaRoot in its default setup (release dec18p1) the particle gun was used. The particle gun is a feature in the PandaRoot framework which gives the user the opportunity to shoot any pre-defined particle into the detector at a given momentum and angle. It requires the DPG number, the angles theta and phi as well as the energy as an input. This information is then handed over to the simulation.

5.1.1 Barrel

The configuration and simulation of photons with different energies hitting the barrel is described in this section. In our case the particle gun was set up to shoot photons into the barrel at the position where the prototype PROTO120 is placed with the goal to compare the simulation with the experiment.

PROTO120 is the most recent real-size prototype representing a section of a barrel slice. It is an upgrade of the previous prototype PROTO60 and contains the most tapered crystals and close to final mechanical components. It consists of 120 lead tungstate ($PbWO_4$) second generation (PWO-II) crystals in total which are read out by the LAAPD's and the signal is processed separately with the custom made APFEL-ASIC. [25] A visualisation of the prototype and the setup is shown in fig. 5.1.

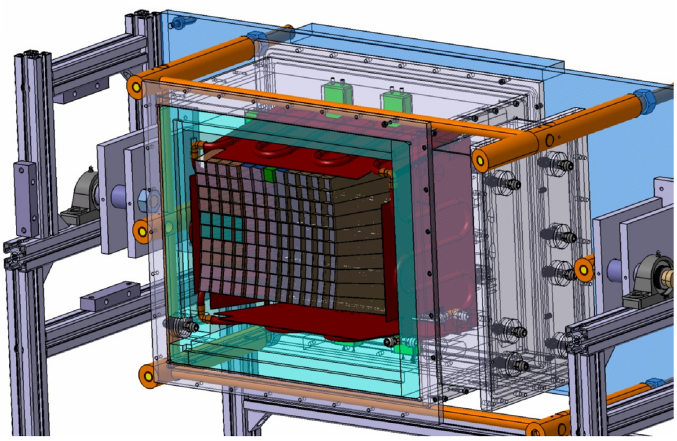

Figure 5.1: Schematic view of the prototype PROTO120 and its mounting. [25] This setup was used to determine the resolution which is used as a reference.

Out of experiments at the MAMI[1] facility in Mainz an energy resolution formula was generated. This will be the reference for further comparisons and calculations. The simulation was therefore adjusted to resemble the experimental setup. The exact values which were used for the particle gun shooting at PROTO120 can be found in table 5.1.

particle	DG number	θ	ϕ
photon (γ)	22	76.25°	180.8°

Table 5.1: Initial values used for the particle gun to hit PROTO120

This setup provides the best possibility to later compare with the PROTO120 since the photons are shot at the same position which was used for prototype tests. Furthermore, they hit the middle crystal of PROTO120 directly into the centre so that there are optimal conditions for an electromagnetic shower with considerably low energy loss. Eleven different energy values starting at 50 MeV reaching up to 15 GeV were simulated with the particle gun shooting into the barrel, while each energy value was simulated with 50,000 events to reduce the statistical error. The hit position with regard to the angles θ and ϕ is shown in figure 5.2. The *eventDisplay* included in PandaRoot was used to generate these visualisations.

[1]Mainzer Mikrotron (MAMI)

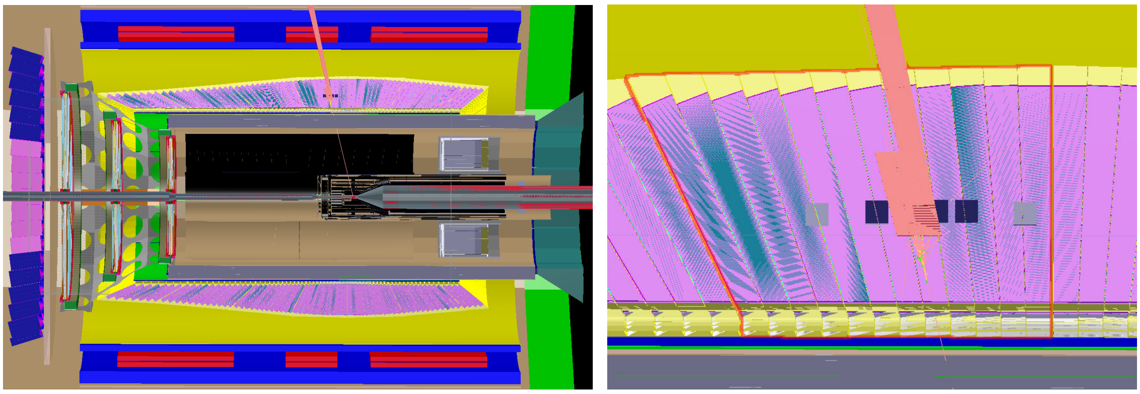

(a) Clipped view from above

(b) Hit into PROTO120 (outlined in red)

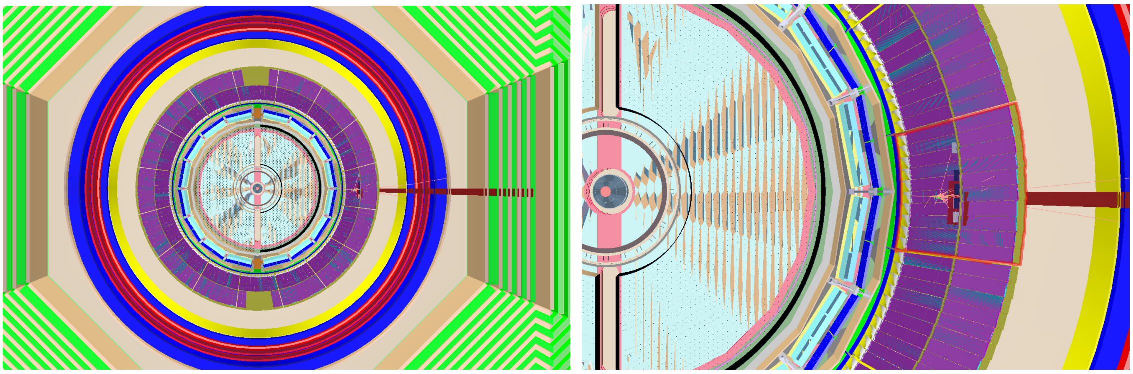

(c) Clipped view from the beam direction

(d) Hit into PROTO120 (outlined in red)

Figure 5.2: Visualisation of the particle gun shooting 1 GeV photons in the direction of $\phi = 180.8°$ and $\theta = 76.25°$. On the left side there is a macroscopic view while the right picture shows a closer perspective with PROTO120 outlined in red. The photons are indicated by a the rose colouring while electrons are marked in yellow and positrons in green. The hit crystals are indicated by the grey cubes while the measured energy is represented by the red beam.

With this setup a full simulation, reconstruction and analysis was executed for each energy. The energy resolution can be calculated by histogramming the photon energy spectrum. These plots are then successively fitted with the Novo-Fit and the fitting macro calculates the energy resolution as described in section 3.5 where the error is determined through error propagation. An exemplary fit is shown in fig. 5.3.

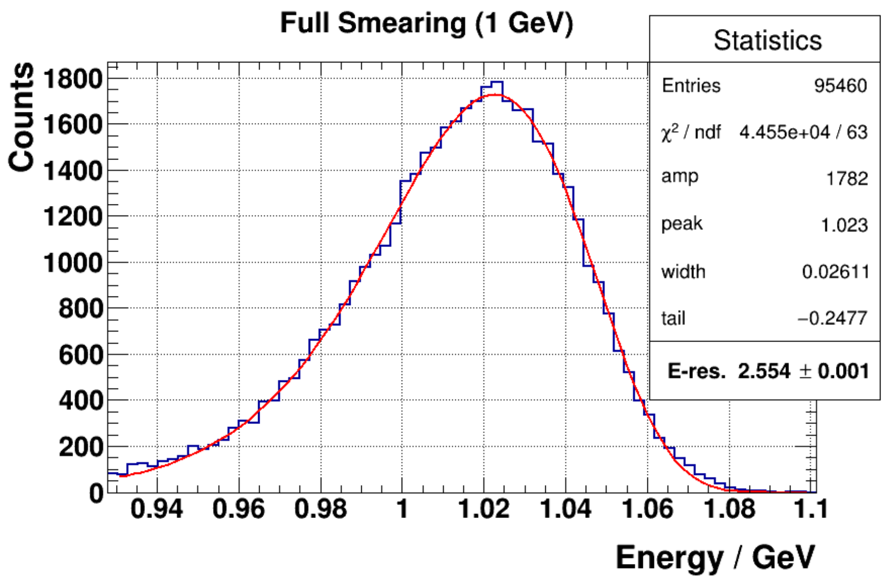

Figure 5.3: Energy peak for 1 GeV photons hitting the barrel simulated with default PandaRoot. The peak is fitted with the Novosibirsk function.

The plot shows that the peak does not match the energy of the initial photons emitted by the particle gun. This is the case for all the simulated energies as shown in table 5.2. It is an effect which results, inter alia, out of the non linear light accumulation in tapered crystals which is implemented in PandaRoot. This will be discussed in more detail later. Furthermore, an incorrectly implemented energy correction algorithm is shifting the values since the highest reconstructed energy in the histogram would normally almost be at the energy of the initial photon. Due to the conservation of energy the default reconstructed energy can in principle not be higher than the incoming energy. However, the energy correction should align the peak position with the energy of the impinging photon. This issue is already known by the $\overline{\text{P}}$ANDA collaboration and developers are working to fix it. Even though the peak position is a coefficient used when determining the energy resolution this issue does not affect the calculated resolution since the values are just multiplied by a factor which affects both width and the peak position in the same way. Therefore, the resulting resolution is not affected by the peak shift.
The statistics box displays all the fitting parameters of the Novo-Fit calculated by the fitting macro. The parameter errors are neither displayed nor taken into account at further calculations since they are considerably small (about three orders of magnitude smaller) and the values obtained from the simulation are generally based on a high statistics with 50.000 events. The large number of events also lead to a negligence of the statistical errors when applying the Novo-Fit. This massively improved the alignment of the fitted function with the simulated data.
Despite the partly small energy resolution error which is calculated through propagation of uncertainty shown in the following tables, the resulting value is often still not perfectly accurate. This is because changing the fitting region can also alter the value of the energy resolution calculated by the fit. This error is hard to estimate in error calculation since

its only dependant on the initial fitting parameters entered by the user. As a way to cope with this issue a similar fitting range was used for each fit and just scaled according to the energy so that the remaining error can be estimated to around $\pm 1\%$. This value is derived from testing different fitting ranges. Table 5.2 shows the gathered data of all simulated energies fitted with the Novosibirsk function and the respective errors calculated with error propagation.

γ energy / GeV	peak reconstructed energy / GeV	σ/E /%	$\Delta(\sigma/E)$ /%
0.05	0.05165	9.4740	0.001209
0.10	0.1022	7.0719	0.000868
0.20	0.2051	5.1049	0.000895
0.50	0.5112	3.3496	0.000605
1.00	1.023	2.5536	0.000504
2.00	2.033	2.2096	0.000464
3.00	3.067	2.0061	0.000458
5.00	5.112	1.9624	0.000448
8.00	8.15	1.8598	0.000464
12.0	12.11	1.8535	0.000486
15.0	15.09	1.8490	0.000527

Table 5.2: Energy Resolution values of the PandaRoot barrel EMC in its default setup simulating the whole $\overline{\text{P}}$ANDA detector including all other sub-systems in front.

After obtaining the different energy resolution values the general energy resolution formula is fitted through the dataset. This formula was already discussed in section 3.4. The result of this fitting function applied on the simulated values is displayed in figure 5.4. It resembles the response curve of the PandaRoot EMC in the default setup. All values on the energy range were taken into account, but the errors were neglected and every data point weighted the same. This was done due to a better fit result.

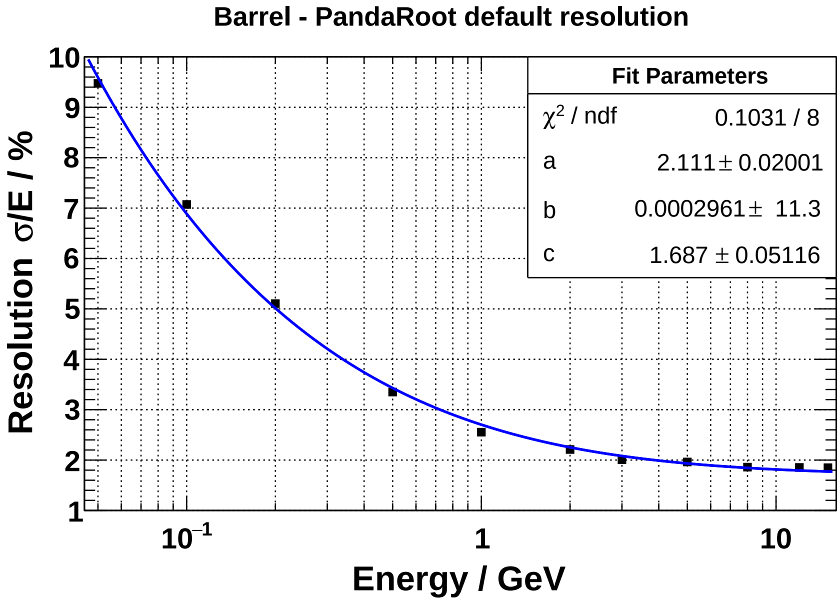

Figure 5.4: Response curve of the barrel EMC when the whole detector is simulated with the default PandaRoot setup.

The fitting parameters shown in the statistics box resemble the coefficients of the energy resolution formula. The curve is in good agreement with the data points which especially becomes clear through the logarithmic scaling of the x-axis. These coefficients already indicate, in comparison to obtained values with prototypes, that the model of the read out in PandaRoot does not match with experimental values.

In this simulation the full detector was generated which complicates the comparison with the experiment. Since the experiment at the MAMI facility was conducted without any interference between the photon beam source and the calorimeter prototype, another simulation was started. In this case only the EMC was simulated so that the photons of the particle gun directly hit the calorimeter. This is visualised in figure 5.5 using the event display where a hit of a 1 GeV photon into the middle crystal of PROTO120 is shown. The photons are indicated by the rose colouring while electrons are marked in yellow and positrons in green. The red beam indicates the energy measured in the corresponding crystal while the *EmcHit*s are represented by the grey cubes. The corresponding line shapes of the peaks over the entire energy spectrum can be found in the appendix in fig. 6.8.

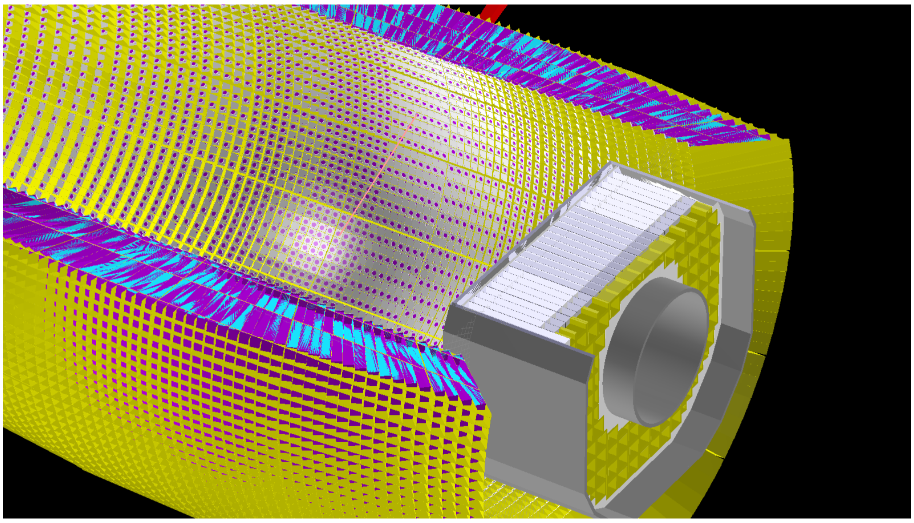

(a) Clipped view of the simulated calorimeter showing the barrel and the backward endcap.

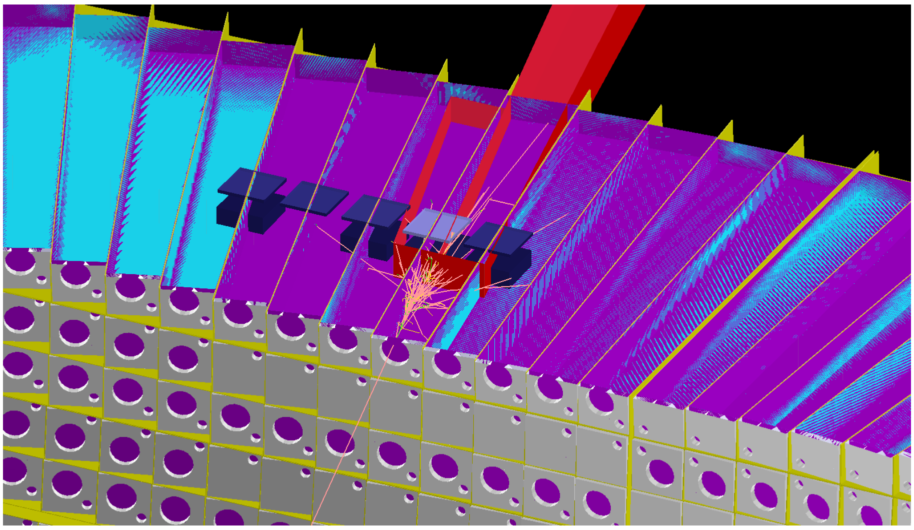

(b) Hit into a clipped PROTO120 crystal.

Figure 5.5: Visualisation of the particle gun shooting $1\ \mathrm{GeV}$ photons at the barrel EMC.

With this altered setup the whole process was repeated. In this case further energy values have been simulated to obtain a more detailed representation. The following response curve shown in fig. 5.6 was obtained. As a comparison the energy resolution formula from experiments with PROTO120 [25] is given in equation 5.1 and also visualised in the plot as a dashed red line.

$$\left(\frac{\sigma}{E}\right)_{PROTO120} = \frac{2.46\ \%}{\sqrt{E/\ \mathrm{GeV}}} \oplus \frac{0.16\ \%}{E/\ \mathrm{GeV}} \oplus 2.32\ \% \qquad (5.1)$$

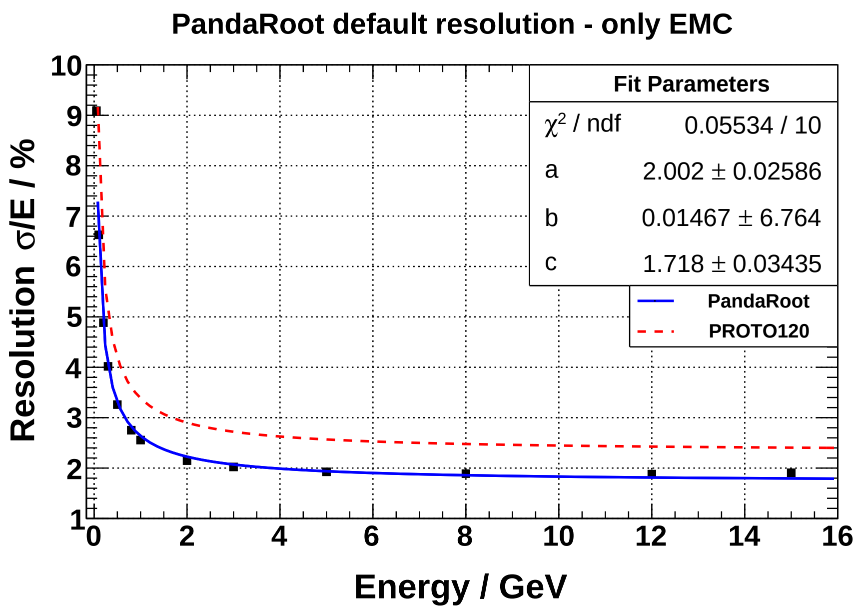

Figure 5.6: PandaRoot default barrel response curve simulating only the EMC (blue) compared to the experimental data (red).

The fitting parameters of the response function through the data points are shown in the statistics box. They resemble the three function coefficients which results in an energy resolution formula given by equation 5.2.

$$\left(\frac{\sigma}{E}\right)_{DefaultBarrel} = \frac{2\ \%}{\sqrt{E/\ \mathrm{GeV}}} \oplus \frac{0.01\ \%}{E/\ \mathrm{GeV}} \oplus 1.72\ \% \tag{5.2}$$

The plot with the corresponding energy resolution formula shows clearly that the experimental data does not match the PandaRoot resolution, neither in the high energy range nor in the low energy region. The resolution is constantly better than expected which means the simulated values are below the experimental ones. This can also be illustrated by the single coefficients since every parameter of the simulated response function is smaller than the experimental one.

With this result it becomes clear that the two resolutions are not matching. This raises the necessity to find a way to match them properly. Before starting to approach this problem another vital part of the EMC was tested to investigate the extent of this discrepancy, the forward endcap.

5.1.2 Forward Endcap

Since the Forward Endcap of the $\overline{\text{P}}$ANDA electromagnetic calorimeter consists of different components compared to the barrel it has also a variant energy resolution. The main differences lay in the readout electronics, because the forward endcap uses vacuum photo tetrodes for the inner most detectors instead of the LAAPDs utilised in the barrel, which furthermore has different preamplifiers and crystal geometries. This consideration lead to another resolution comparison of the forward endcap simulation with experimental data.

The latest prototype data was obtained in 2012 with a test setup which was measured using beams at the MAMI facility for low energies and at CERN for high energies. The prototype consists of 216 non-tapered PWO-II crystals. It represents a cutout of the forward endcap at the top left edge to the elliptical hole in the centre of the detector as shown in fig. 5.7. The tests were performed at the envisaged environment temperature of $T = -25\ ^\circ\mathrm{C}$ to analyse the performance in the most realistic scenario.[10]

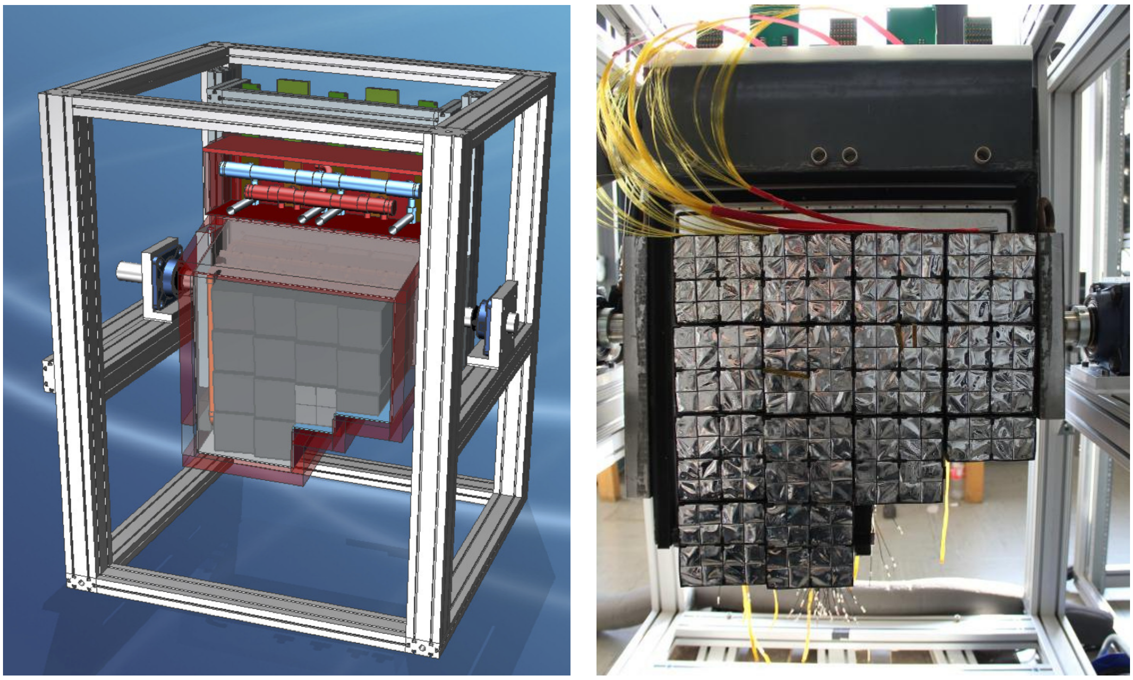

Figure 5.7: Left: CAD drawing of the Forward Endcap prototype; Right: prototype as it is fully assembled.[10]

The data which was obtained at this measurement can be found in fig. 5.8. In this plot the dotted line in blue is not a fit, but the envisaged energy resolution from the $\overline{\text{P}}$ANDA Electromagnetic Calorimeter Technical Design Report[9]. The black data points are those obtained at the MAMI facility while those in red and green were measured at the CERN Super Proton Synchrotron.

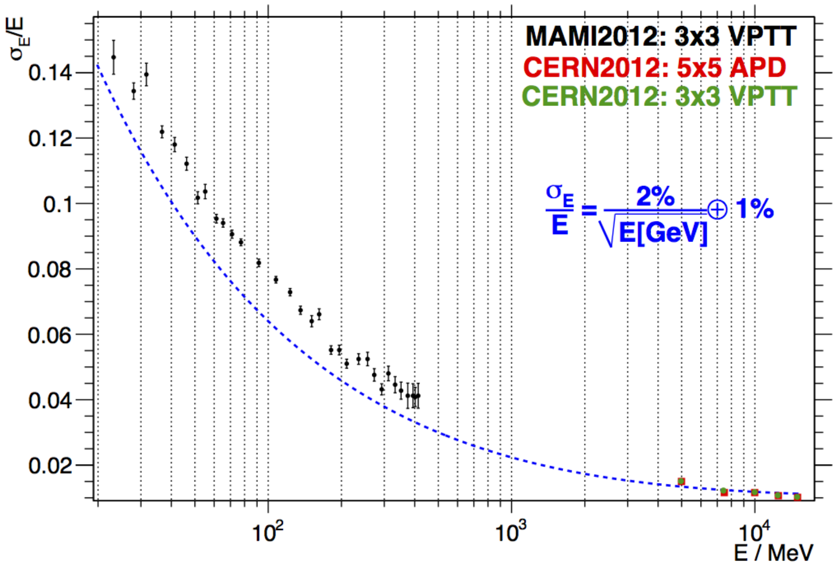

Figure 5.8: Energy resolution as a function of beam energy. The blue curve shows the envisaged energy resolution. [10]

Since the dashed blue TDR curve in the plot obviously does not represent the measured response curve the individual data values from this test setup were fitted. The utilised fitting function was again the energy resolution formula discussed in section 3.4. In the fit displayed in fig. 5.9 all data points were weighted the same because this improved the resulting alignment with the data points.

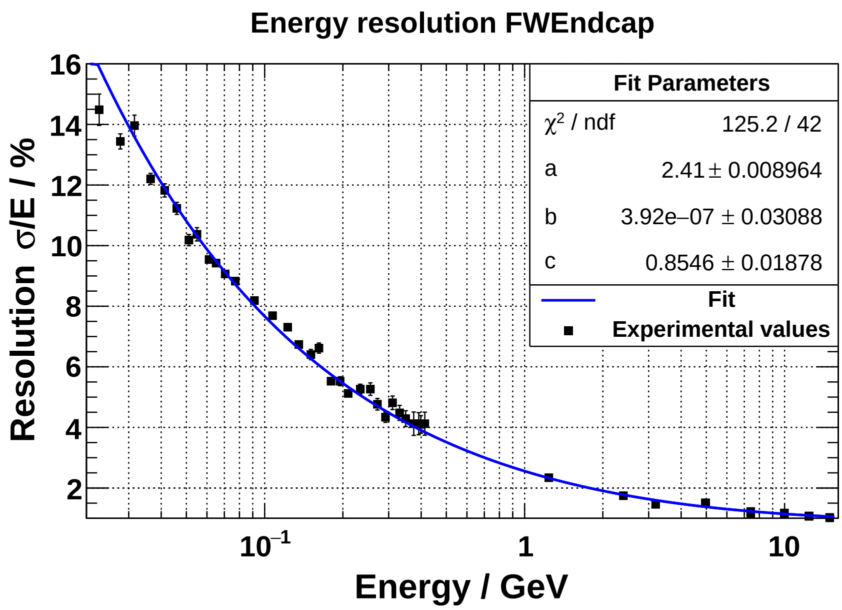

Figure 5.9: Response curve of the forward endcap with data obtained at prototype experiments.

This fit resulted in an energy resolution formula given by eq. 5.3.

$$\left(\frac{\sigma}{E}\right)_{ProtoFWEndcap} = \frac{2.41\ \%}{\sqrt{E/GeV}} \oplus \frac{4 \cdot 10^{-7}\ \%}{E/GeV} \oplus 0.85\ \% \approx \frac{2.41\ \%}{\sqrt{E/GeV}} \oplus 0.85\ \% \qquad (5.3)$$

To test and compare the resolution of PandaRoot to these experimental data the particle gun was used once again. To visualise the simulated forward endcap fig. 5.10 shows a lateral perspective of the EMC in pink and the barrel muon detector for scale. The individual blocks with a pink rhombus pattern on the front face may be falsely seen as single crystals. However these are the alveoles containing a set of 4x4 crystals each so that the forward endcap EMC totally consists of 3864 crystals.

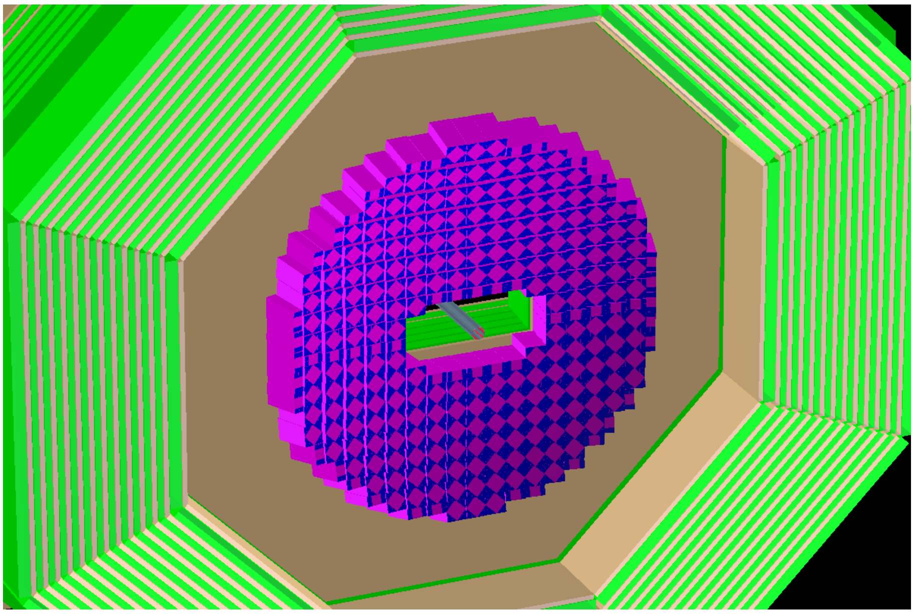

Figure 5.10: Lateral view on the forward endcap EMC (pink) containing the envisaged 3864 crystals.

As in the final comparison of the barrel response curves the tests were performed simulating only the EMC. This time the hit position of the fired photons was aligned with the forward endcap prototype test. It is displayed in fig. 5.11. The impact photon is painted in light rose while the red beam is an indicator for the measured energy.

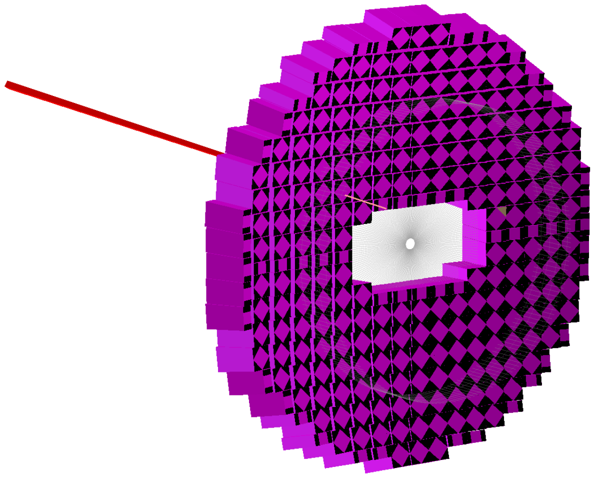

Figure 5.11: Hit position of the photons used for testing the forward endcap energy resolution.

As in previous tests photons with specific energy values in the range of 50 MeV to 15 GeV were shot at this position. After running a full simulation, reconstruction and analysis the resulting energy peaks were subsequently fitted with the Novosibirsk function to calculate the energy resolution. An exemplary fit is shown for 1 GeV photons in fig. 5.12.

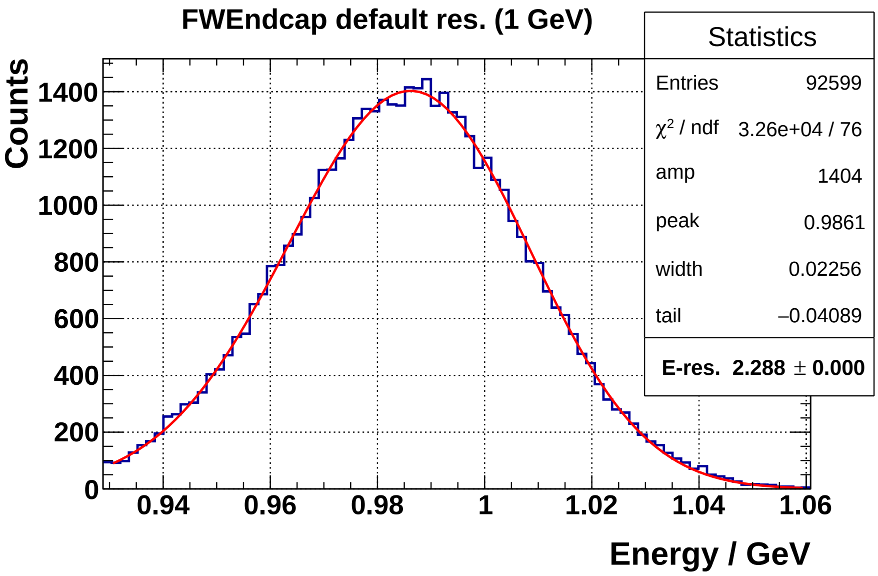

Figure 5.12: Energy peak for 1 GeV photons hitting the forward endcap fitted with the Novosibirsk function.

The error of the energy resolution is displayed as zero but actually it is just smaller than 0.0005. It is calculated through error propagation as discussed in section 3.5. The values obtained from the simulation are generally based on a high statistics with 50.000 events which leads to a negligence of the statistical error as done at the barrel. The error emerging from changing the fitting region by the user can also be estimated by $\pm 1\%$. Table 5.3 shows the data calculated by the Novo-Fit.

γ energy / GeV	peak reconstructed energy / GeV	σ/E /%	$\Delta(\sigma/E)$ /%
0.05	0.0490	11.522	0.002115
0.10	0.0974	8.0516	0.001758
0.20	0.1954	5.5991	0.001006
0.30	0.2941	4.4393	0.000845
0.50	0.4916	3.3359	0.000734
0.80	0.7886	2.5803	0.000622
1.00	0.9861	2.2881	0.000475
2.00	1.974	1.6065	0.000351
3.00	2.963	1.3307	0.000266
5.00	4.936	1.0586	0.000238
8.00	7.892	0.8984	0.000217
12.0	11.83	0.8068	0.000207
15.0	14.78	0.7748	0.000169

Table 5.3: Energy Resolution values of the PandaRoot forward endcap EMC in its default setup.

These values can now be fitted using the general energy resolution formula. In fig. 5.13 the fitted function is compared to the response curve which was determined earlier with data from the prototype tests. The plots clearly show that, in contrast to the default barrel resolution, the two response functions are matching very well in the lower energy spectrum up to 1 GeV shown in fig. 5.13(a). At this point the experimental resolution starts to get worse than the simulated response. This effect increases throughout the upper energy range so that there is a significant difference for high energetic photons.

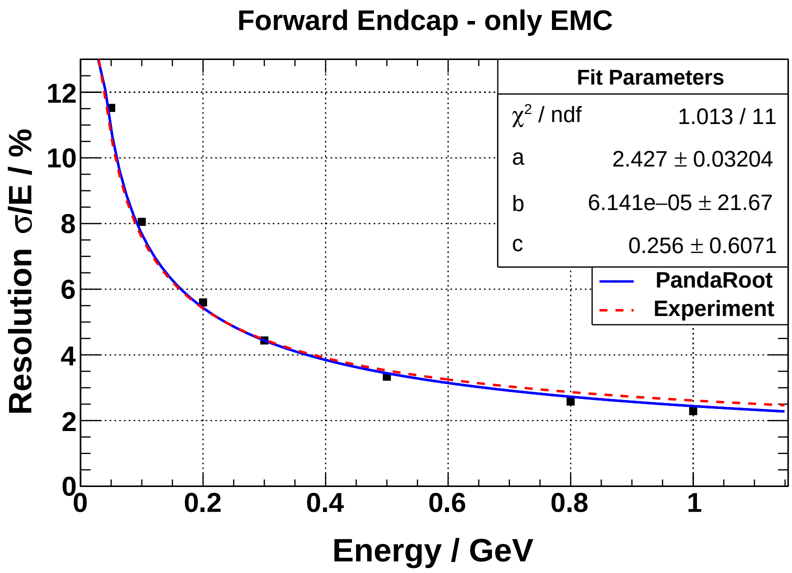

(a) lower energy spectrum

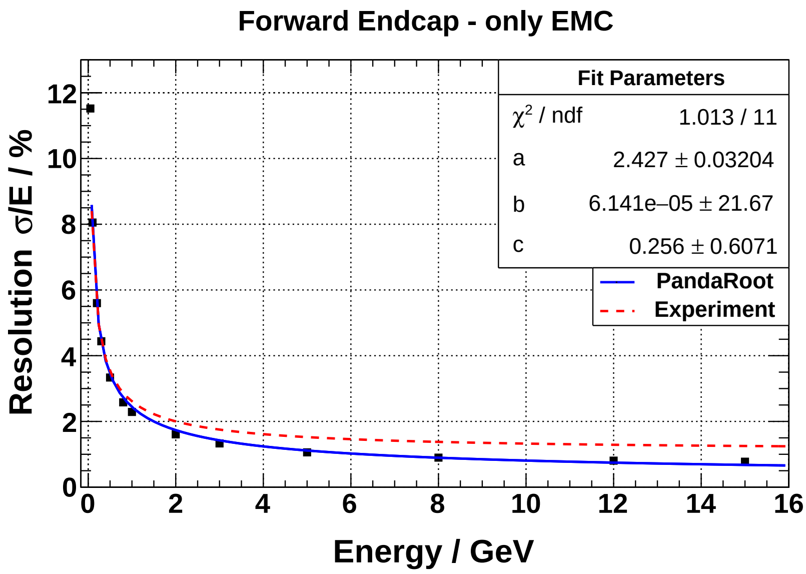

(b) full simulated energy range

Figure 5.13: Response curve of the PandaRoot forward endcap EMC in its default setup (blue) and the prototype tests (red).

The resulting energy resolution of the default PandaRoot forward endcap EMC is given by:

$$\left(\frac{\sigma}{E}\right)_{DefaultFWEndcap} = \frac{2.43\ \%}{\sqrt{E/\ \mathrm{GeV}}} \oplus \frac{6 \cdot 10^{-5}\ \%}{E/\ \mathrm{GeV}} \oplus 0.26\ \% \tag{5.4}$$

Regarding the conducted tests and comparisons it becomes clear that the experimental and simulated resolution again does not match. This phenomenon is more prominent at the barrel EMC than at the forward endcap since the barrel resolution is constantly too good as shown in fig. 5.6. However, both modules put out wrong results for energies higher than 1 GeV. This is a crucial flaw since the correct simulation of the the detector is necessary for future testing and analysis. Therefore, it is dependant on the conformity with the experiment. This results in the need to find a way to align both response curves properly.

5.2 Calculation of the energy resolution

As discussed in the previous section the non-compliant response curves of PandaRoot and the experiments have to be matched. The first step to achieve this is to take a closer look at the part of the simulation which is responsible for the smearing of the "measured" energy values. In chapter 4 the data flow of PandaRoot concerning the EMC was discussed. It became clear that the energy resolution is added in the digitisation model which is split into two different paths as shown in fig. 4.2. The default way which was also used for simulating the data of the comparison tests is the *real digitisation*. It creates waveforms out of the hits and those digitised. After a deep look into the code all the factors involved into creating the smearing of a hit could be obtained and are visualised in fig. 5.14. The task only happens in `PndEmcHitsToWaveform`.

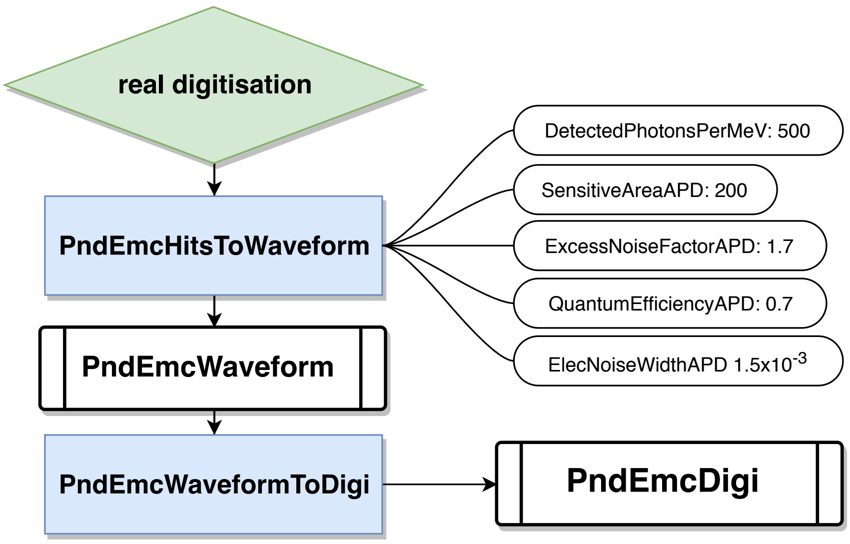

Figure 5.14: Segment of the PandaRoot data flow showing the real digitisation path and the inputs used for smearing.

The figure shows the individual coefficients and the corresponding value in case of the barrel. The calculation in the real digitisation is based on the theory of the resolution of an electromagnetic calorimeter. The program is replicating the process which is happening in a real calorimeter using the theoretical description which was discussed in chapter 3. In PandaRoot the first Gauss smearing is applied on the hit energy which calculates the amplitude. In case of the barrel the standard deviation is given by eq. 5.5. This represents in principle the stochastic term a of the energy resolution formula. The calculation is similar for the other parts of the calorimeter.

$$\sigma = a = \sqrt{\frac{F}{1000 \cdot E \cdot N_e}} \tag{5.5}$$

$$N_e = LY \cdot \frac{A_{APD}}{745\ \mathrm{mm}^2} \cdot QE_{APD} \tag{5.6}$$

In this case the variables of fig. 5.14 were exchanged with formula symbols were E resembles the energy, F the `ExcessNoiseFactorAPD`, N_e the `NPhotoElectronsPerMeVAPDBarrel` which is calculated out of the variables `DetectedPhotonsPerMeV` (LY), `SensitiveAreaAPD` (A_{APD}) and `QuantumEfficiencyAPD` (QE_{APD}). The last equation is responsible for calculating the number of photoelectrons in the APD or VPT, where LY represents the number of photons at the crystal end-face, A the active area of the APD and QE its quantum efficiency. To estimate the actual number of photoelectrons in the barrel crystals the rear surface is taken equal for all the crystals. This results in an average of $745\ \mathrm{mm}^2$, however it varies depending on the type of the crystal. For forward and backward endcap rear surface is equal to $26\ \mathrm{mm} \cdot 26\ \mathrm{mm} = 676\ \mathrm{mm}^2$ for all crystals. Depending on the part of the EMC the corresponding values are exchanged. With the values utilised in the default version of PandaRoot the stochastic term for the barrel calculates to:

$$a = \sqrt{\frac{1.7}{1000 \cdot 500 \cdot \frac{200\ \mathrm{mm}^2}{745\ \mathrm{mm}^2} \cdot 70\%}} = 0,425\ \% \tag{5.7}$$

This value does already not match with the stochastic term of the PROTO120 given in eq. 5.1. Afterwards the electronic noise is added using the noise width of the respective component. In the case of the APD this is done with the preset value `ElecNoiseWidthAPD` $= 1.5\ \mathrm{MeV}$. This process of successively adding different smearing ultimately results in the deviation of the calculated energy resolution from the experimental values.

5.3 First approach to correct the energy resolution

After examining the mechanisms of the *real digitisation* the first approach was to revise the values used in the parameter file. The idea was to check and change the parameters to a reasonable extent to align the resolution with the experiment. However, the light yield, the quantum efficiency and the noise width of the APD were preset values which were gained experimentally or clearly specified in the data sheet. Technically the excess noise factor

F is also limited to a certain range of 2.5 to 3.1 according to the data sheet [26]. But this value is applicable at 20 °C and a gain of $M = 100$. Due to an environment temperature of -25 °C and an envisaged gain of $M = 150$ the excess noise factor might exceed those limits and can be estimated using eq. 5.8:

$$F(M) = kM + (1-k)\left(2 - \frac{1}{M}\right) = 0.02 \cdot 150 + (1 - 0.02)\left(2 - \frac{1}{150}\right) = 4.95 \approx 5 \quad (5.8)$$

In this case $k = 0.02$ is the ionisation ratio of silicon.[27] In comparison to the original excess noise factor of $F = 1.7$, this is a significant difference. Another value which could be changed is the sensitive area of the APD since $200\ \mathrm{mm}^2$ is only an approximation. As fig. 5.15 shows the actual sensitive area of the two APDs calculates to a value of $6.8\ \mathrm{mm} \cdot 14\ \mathrm{mm} \cdot 2 = 190.4\ \mathrm{mm}^2$

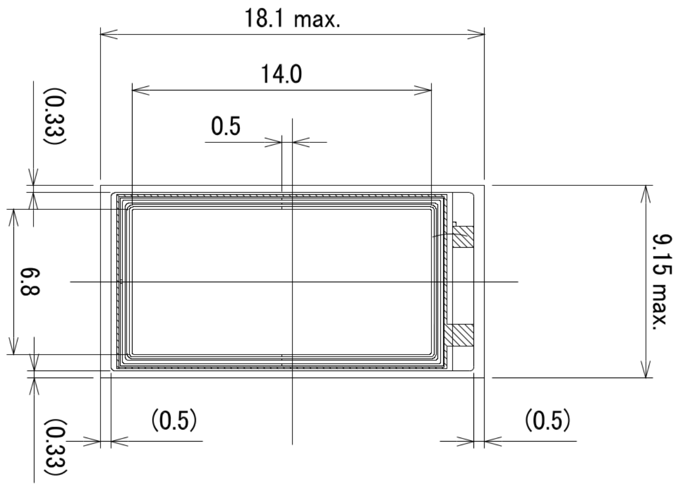

Figure 5.15: Technical drawing of the front face of the utilised APDs. All values are in mm [26].

With this significant change to the excess noise factor and the adjustment of the sensitive area the stochastic term of this *parameter approach* is given by:

$$\sigma = a = \sqrt{\frac{5}{1000 \cdot 500 \frac{190.4\ \mathrm{mm}^2}{745\ \mathrm{mm}^2} \cdot 0.7}} = 0,748\ \% \quad (5.9)$$

Despite the modifications the value did not chance significantly compared to the stochastic term of the PROTO120. After running a full simulation at low energies where the discrepancies are especially visible, it became clear that changing the parameters was not leading to the correct results. However, further changing the parameters might end up being not physically reasonable any more.

Apart from that, the ground up theoretical calculation in the real digitisation does not compensate the intrinsic GEANT resolution correctly when the smearing is added. When

particles pass through the detector simulated with GEANT they are also subject to some smearing due to effects occurring at the interaction with other parts of the detector or general energy loss. This has to be considered when the resolution is artificially added in the digitisation. Furthermore the simulation is assuming perfectly calibrated crystals so no calibration errors are present which would contribute to the constant term of the response function.
These reasons demonstrate the need to rethink the digitisation. This is why another attempt with a transition to a more straight forward approach was started. The detailed execution is described in the next section.

5.4 Alternative method using the ideal digitisation

In the last section it became clear that the first approach using the default digitisation path with adjusted parameters did not result in a reasonable match with the experiments. The new approach is based on a different way of digitising the hits. In this case the existing *ideal digitisation* of fig. 4.2 was modified and used. The ultimate goal is to smear the resolution exactly according to the formula obtained at experiments with prototypes like the PROTO120. This way the simulated results should match the experimental data way better than in a pure theoretical approach as used in the real digitisation model. Fig. 5.16 shows that instead of the hits being transformed into waveforms before being fully digitised the new ideal digitisation path digitises the hits directly. In the code the module of hit which is handed over to the digitisation is checked and according to this information a specific smearing formula can be applied.

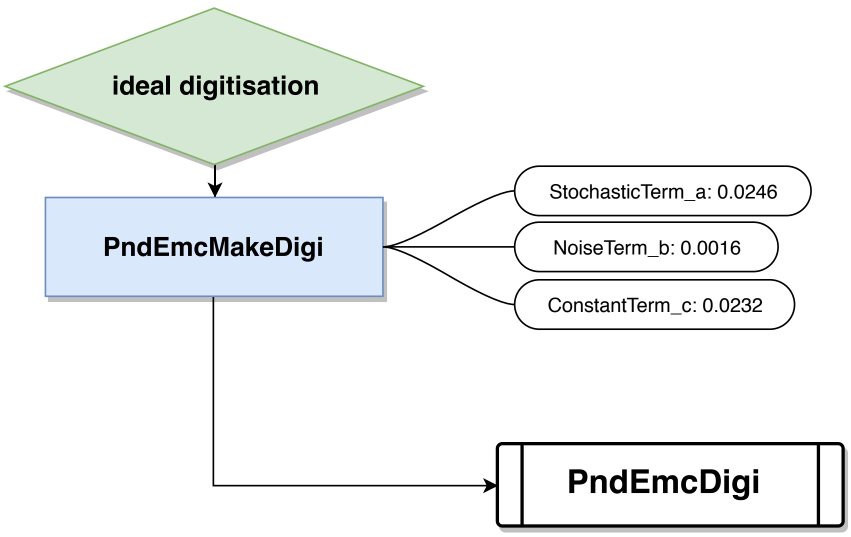

Figure 5.16: Segment of the PandaRoot data flow showing the ideal digitisation path and the inputs used for smearing with the corresponding values for the barrel.

The figure shows the goal of this altered digitisation path. It is envisaged to smear the events according to the empirical formula where the three coefficients are just provided as an input in the parameter database. Applying this way of digitising, the process is faster and also simpler which provides more clarity in the complex PandaRoot code.

5.4.1 Barrel

Before starting to change the digitisation simply according to the barrel response curve a few considerations are of great importance. It was already mentioned that GEANT gives an intrinsic resolution. This is due to statistical shower fluctuations and energy losses. Obviously this already happens in the GEANT simulation so that the digitisation would ultimately add too much noise by smearing the values according to the PROTO120 formula. This also means when there is no smearing added at all, the measured peak will still have a certain distribution.
Another factor adding to this distribution is the non-linear light collection implemented in the `PndEmcHitProducer` shown in fig 4.2. Since the barrel crystals have a tapered geometry, simulations and initial measurements have shown that the light yield at the same deposited energy depends on the location of the deposition in the crystal. Experiments demonstrated that the number of scintillation photons of a 1 MeV gamma source detected by a photosensitive detector increases with the distance of the source along the crystal to the photosensor. This, at first sight astonishing result, arises from a complicated interplay of self-absorption in the scintillator material and reflected photons at the interfaces of the lead tungstate crystal. The different crystal geometries must be taken into account, because the larger the crystal shape deviates from a rectangular geometry, the stronger the effect.[28] These effects lead to a certain energy resolution which exists without any smearing in the digitisation. This will later be referred to as the *GEANT resolution*.

Consequently, the first step to use the altered digitisation path is to determine the GEANT resolution. Therefore, the particle gun was set up again to shoot into the barrel at the same position as in the previous simulations indicated in fig. 5.5. To achieve similar conditions as in the experiments only the EMC was simulated. The fits were again performed with the Novosibirsk function leading to the energy resolution values shown in table 5.4.

γ energy / GeV	σ/E /%
0.05	6.0818
0.10	4.4830
0.20	3.4135
0.30	2.9019
0.50	2.4729
0.80	2.1889
1.00	2.0916
2.00	1.9031
3.00	1.8499
5.00	1.8323
8.00	1.8365
12.0	1.8522
15.0	1.8735

Table 5.4: Energy Resolution values of the PandaRoot barrel EMC with no smearing added in the digitisation (GEANT resolution).

These values were again fitted to obtain a general response curve of GEANT in the active range of the detector. The energy resolution curve together with the fit parameters are shown in fig. 5.17. In this plot the energy axis is scaled logarithmically to receive a better view on the fit on the whole range, especially considering the small energies.

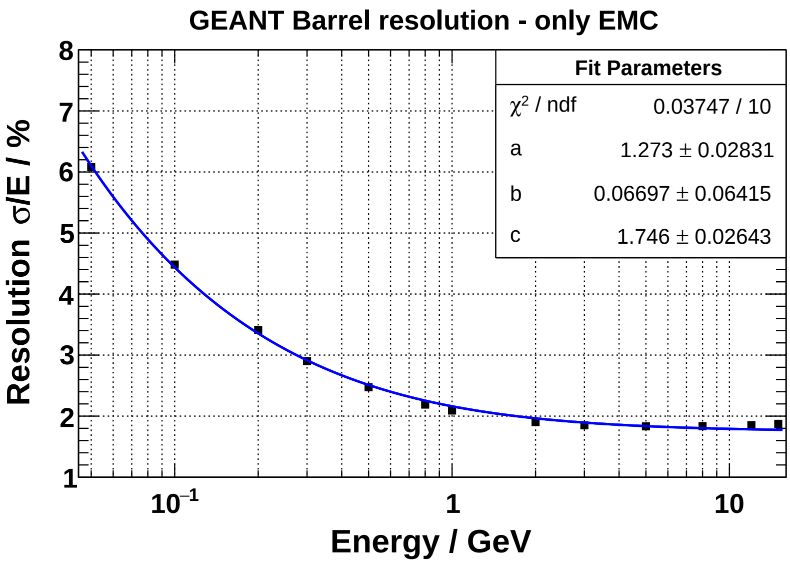

Figure 5.17: Response curve of the PandaRoot barrel EMC with no smearing performed in the digitisation model (GEANT resolution). The errors of the resolution are smaller than 0.001 and therefore negligible.

The corresponding energy resolution is given by:

$$\left(\frac{\sigma}{E}\right)_{GEANT\_Barrel} = \frac{1.27\ \%}{\sqrt{E/\ \mathrm{GeV}}} \oplus \frac{0.07\ \%}{E/\ \mathrm{GeV}} \oplus 1.75\ \% \tag{5.10}$$

This expression can now be used to calculate the remaining smearing which has to be added in the digitisation. The PROTO120 formula outputs the relative energy resolution at a certain energy of photons hitting the prototype, or in our case, the barrel. This means that the simulated smearing which happens in GEANT is already included. To apply this formula to the digitisation the approach is to subtract the obtained GEANT resolution from the desired resolution. This leads to the desired smearing which has to be performed in the digitisation. Since combining energy resolutions is done by quadratically adding them the calculation, the solution to this issue is to quatratically subtract the noise created by GEANT as shown in equation 5.12:

$$\left(\frac{\sigma}{E}\right)_{PROTO120} \stackrel{!}{=} \left(\frac{\sigma}{E}\right)_{simulation} = \left(\frac{\sigma}{E}\right)_{GEANT} \oplus \left(\frac{\sigma}{E}\right)_{digitisation} \tag{5.11}$$

$$\Rightarrow \left(\frac{\sigma}{E}\right)_{digitisation} = \sqrt{\left(\frac{\sigma}{E}\right)^2_{PROTO120} - \left(\frac{\sigma}{E}\right)^2_{GEANT}} \tag{5.12}$$

With these considerations the digitisation path was changed to the introduced ideal digitisation. The energy of the hits was then smeared according to equation 5.12 with the previously obtained GEANT barrel resolution and the PROTO120 formula. Apart from that, the same energetic values and particle gun setup as in the previous simulations was used. The simulation was again started with only the EMC being activated in the code. This also gave the possibility to ultimately compare the response with the experiment since the overall conditions are matched. The resulting values can be found in table 5.5 where also the corresponding values calculated with the prototype formula are listed. The line-shapes can be found in the appendix in fig. 6.9.

γ energy / GeV	(σ/E) /%	$(\sigma/E)_{PROTO120}$ /%
0.05	12.55	11.69
0.10	8.872	8.27
0.20	6.416	6.02
0.30	5.340	5.08
0.50	4.380	4.19
0.80	3.652	3.60
1.00	3.412	3.39
2.00	2.895	2.90
3.00	2.696	2.72
5.00	2.573	2.57
8.00	2.472	2.48
12.0	2.433	2.43
15.0	2.436	2.41

Table 5.5: Energy Resolution values of the PandaRoot barrel EMC with the approach of correcting the resolution in the ideal digitisation. The calculated errors of the resolution are smaller than 0.002 and therefore negligible.

These simulated values already show a very good agreement with the experimental data. Due to the nature of the response calculation the lower energies inherently show larger discrepancies. But, especially compared to the previous result of the real digitisation, the simulation is in almost perfect alignment with the experiment as fig. 5.18 visualises. The fit through the simulated values is marked in blue, while the red dashed line represents the PROTO120 prototype formula found in 5.1.

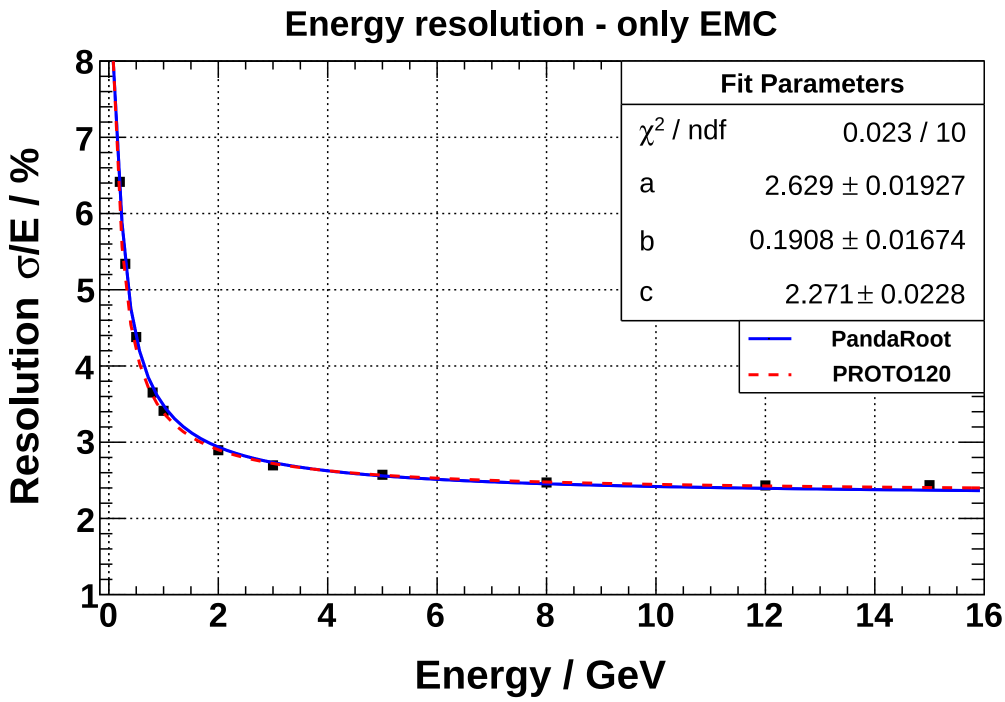

Figure 5.18: Response curve of the PandaRoot barrel EMC with the ideal digitisation path compared to the experimental data.

As the figure above shows the two curves are matching on the whole energy spectrum. As a first conclusion this alternative digitisation path leads to promising results, especially compared to the other way of digitisation in terms of energy resolution. The next step is to apply this procedure onto the forward endcap.

5.4.2 Forward Endcap

Since the ideal digitisation obviously works well for the barrel, the same process was initiated for the forward endcap. The particle gun was set up to shoot 50,000 photons at the predefined position shown in fig. 5.11 with only the EMC being simulated. According to the procedure for the barrel the first task is to determine the GEANT resolution. Therefore, no smearing was added in the digitisation so the peaks accumulating in the measured energy spectrum lead to the resolution which had to be subtracted in the ideal digitisation.

However, the GEANT resolution plots resulting at the forward endcap differ from the ones obtained at the barrel as shown in fig. 5.19. Especially in the lower energy range the plots show a pattern where a delta like peak is positioned at the energy of the initially impinging photon and another smaller but wider peak accumulates in front of that. There is no photon detected which has a higher energy than the primary energy of the originating photon. This is exactly what one would expect due to the conservation of energy.

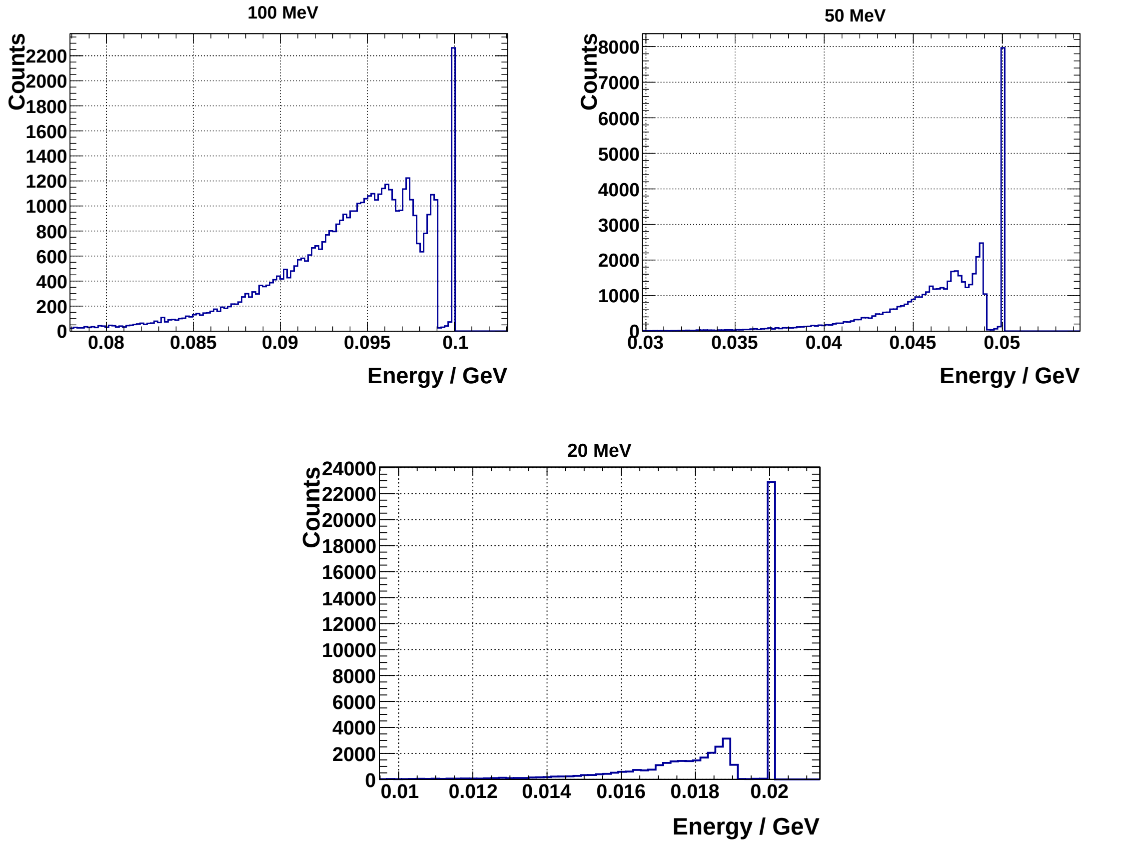

Figure 5.19: Energy peaks for low energetic photons shot into the forward endcap with no smearing in the digitisation.

This shows that in the case of the forward endcap there is no smearing or correction before the digitisation. In contrast to that the barrel readout chain contains the implemented non-linear light collection implemented in the `PndEmcHitProducer` shown in fig. 4.2, which is before the digitisation. As already discussed this correction also leads to some smearing of the energy values so that in case of the barrel the GEANT resolution could be fitted with the Novo-Fit. The displayed low energetic plots of the forward endcap, however, can not be reasonably fitted with the Novo-Fit because even if the fit aligns with the wider peak, the resulting energy resolution would be flawed. This is because later the smearing is added onto all the values, but fitting only the front peak neglects the delta like peak.

Before discussing how to deal with this problem, it is important to investigate where the two different peaks originate from. For this reason the multiplicity of the events was examined. This is the number of crystals responding to a photon hitting the EMC. Figure 5.20 shows the multiplicity plotted for events in the delta like peak and the other wider peak for the simulation of 20 MeV photons. The cut was placed at 19.8 MeV.

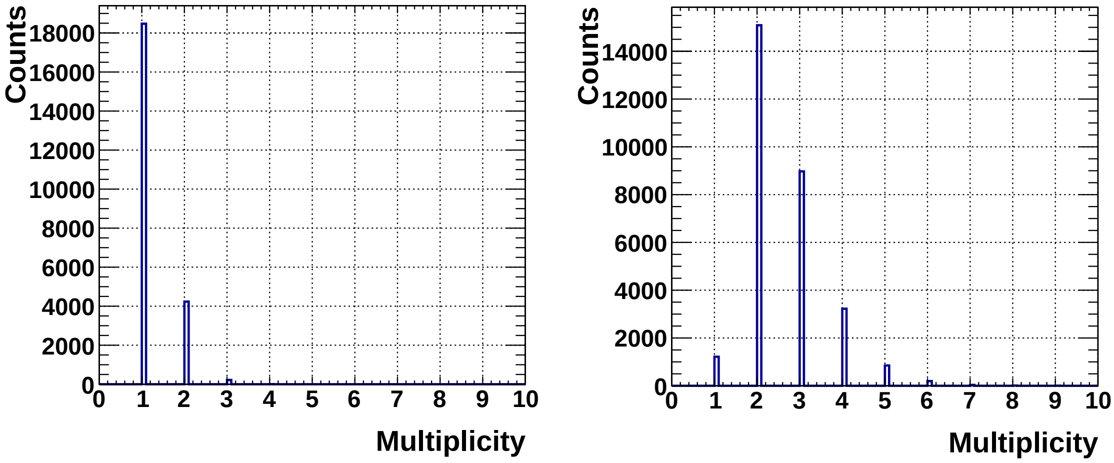

(a) Events from the delta peak

(b) Events from the wide peak

Figure 5.20: Multiplicity plots for the two different peaks at $20\ \mathrm{MeV}$.

These plots indicate, that the delta-like peak is caused by events where the full energy is deposited within the crystals. Due to the very low multiplicity the probability of energy loss in the dead material is rather low. Furthermore, no loss due to backscattering occurred in those events. Since GEANT simulates the energy measurement by determining the energy in a specific volume (in this case this is the crystal volume) there is no statistical smearing if the full energy is deposited. In fig. 5.21 two cases are shown for a shower affecting one crystal compared to a shower spreading onto seven individual crystals. The perspective shows the backside of the forward endcap where the transparency of the crystals is set to 50 %.

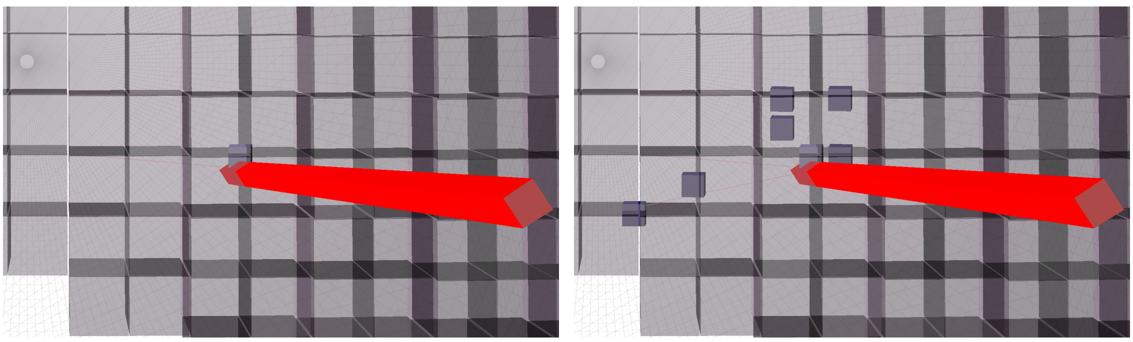

(a) Shower contained in only one crystal

(b) The shower affects seven crystals

Figure 5.21: Electromagnetic shower for different multiplicities.

Obviously this effect causes trouble when determining the GEANT resolution. This is especially the case for low energies since with increasing energy the shower spread enlarges and the effect diminishes. Consequently, the first approach to solve this issue was to neglect the low energetic values because the higher energy peaks could be fitted with the

Novosibirsk function. Subsequently the obtained resolution values from higher energies were fitted with the response curve function. The idea was to extrapolate this curve onto smaller energies to gain a response function which is valid for the whole spectrum. This was implemented into the digitisation and the experimental response function of 5.3 was provided as the desired resolution similar to the barrel ideal digitisation process. However, this leads to no sufficient result causing high deviations from the experimental response after running a simulation. The divergence is visualised in fig. 5.22 which clearly shows that especially the low energetic values do not match.

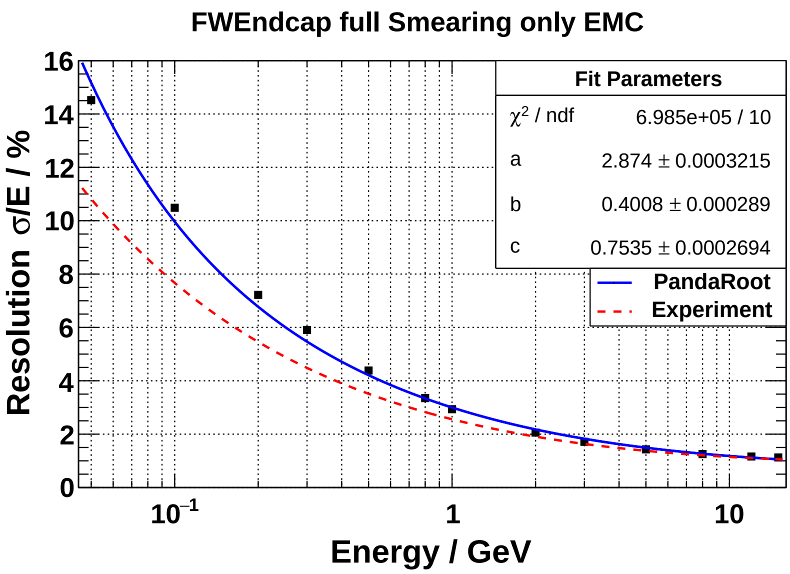

Figure 5.22: Response curve of the PandaRoot forward endcap EMC with the ideal digitisation path compared to the experimental data. The digitisation was performed using the flawed GEANT resolution which was extrapolated from only the high energetic values.

Since extrapolating the GEANT response curve to lower energies did not turn out the desired result several other approaches were started. After other failed attempts including a way to subtract the delta of the graphs shown above or reverse engineering the GEANT resolution out of the existing data, a promising approach was found. The idea was to implement a simple "pre-smearing" in the digitisation. This means to spread the incoming energy values of the GEANT simulation according to a sample smearing formula shown in eq. 5.13.

$$\left(\frac{\sigma}{E}\right)_{sample} = \left(\frac{1\%}{\sqrt{E}}\right) \oplus (0.5\%) \tag{5.13}$$

This sample resolution was intentionally chosen to be very basic and consists of rather small values so that the later performed subtraction of the experimental formula will not end up in complex numbers. Two of the line shapes of fig. 5.19 after adding this pre-smearing can be found in fig. 5.23. It is clearly visible than those can now be fitted with the Novo-Fit.

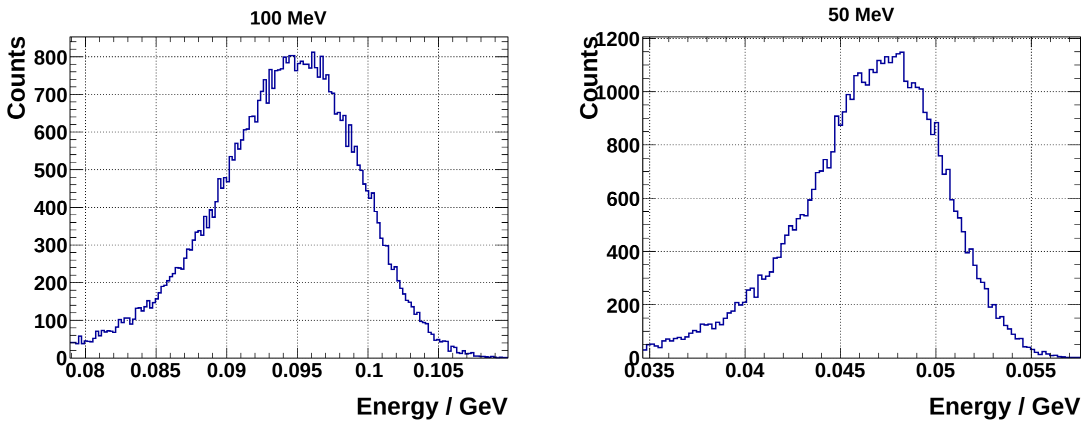

Figure 5.23: Energy peaks for low energetic photons shot at the forward endcap with the basic pre-smearing in the digitisation.

After running a simulation with this formula implemented in the digitisation the following resolution shown in fig. 5.24 was obtained.

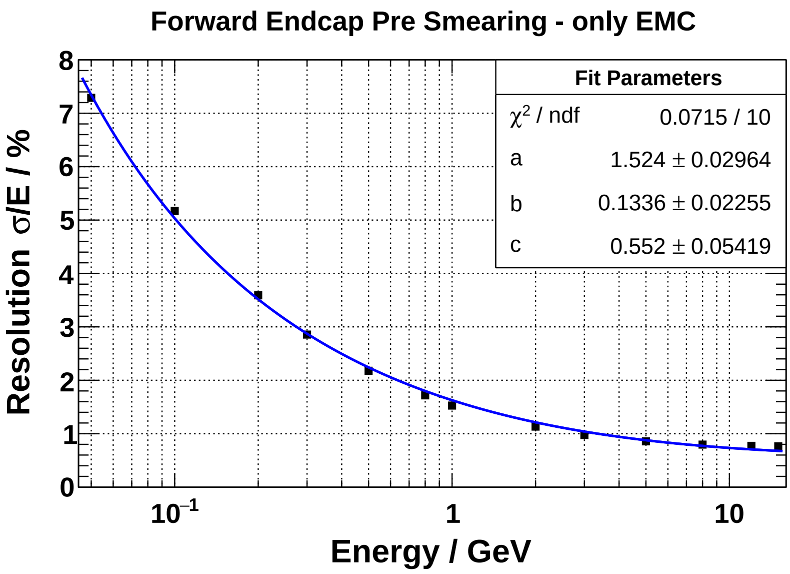

Figure 5.24: Response curve of the PandaRoot forward endcap EMC with a sample pre-smearing implemented into the ideal digitisation path.

This pre-smearing resolution is now composed out of the two factors from GEANT and the sample smearing as eq. 5.14 illustrates.

$$\left(\frac{\sigma}{E}\right)_{preSmearing} = \left(\frac{\sigma}{E}\right)_{GEANT} \oplus \left(\frac{\sigma}{E}\right)_{sample} \tag{5.14}$$

This identity can then be used to deduce the GEANT term by quadratically subtracting the sample term used in the digitisation from the simulated pre-smearing results. This leads to the following expression for the sought GEANT resolution where the "$preS$" coefficients are the fit parameters of fig. 5.24:

$$\left(\frac{\sigma}{E}\right)_{GEANT} = \left(\frac{\sigma}{E}\right)_{preSmearing} \ominus \left(\frac{\sigma}{E}\right)_{sample} \tag{5.15}$$

$$\begin{aligned}
\left(\frac{\sigma}{E}\right)^2_{GEANT} &= \left(\frac{a_{preS}}{\sqrt{E}}\right)^2 + \left(\frac{b_{preS}}{E}\right)^2 + c^2_{preS} - \left(\frac{a_{sample}}{\sqrt{E}}\right)^2 - c^2_{sample} \\
&= \left(\frac{\sqrt{a^2_{preS} - a^2_{sample}}}{\sqrt{E}}\right)^2 + \left(\frac{b_{preS}}{E}\right)^2 + \left(\sqrt{c^2_{preS} - c^2_{sample}}\right)^2 \\
&= \left(\frac{\sqrt{(1,524\%)^2 - (1\%)^2}}{\sqrt{E}}\right)^2 + \left(\frac{0.134\%}{E}\right)^2 + \left(\sqrt{(0.552\%)^2 - (0.5\%)^2}\right)^2
\end{aligned}$$

$$\Rightarrow \left(\frac{\sigma}{E}\right)_{GEANT} = \sqrt{\left(\frac{1.15\%}{\sqrt{E}}\right)^2 + \left(\frac{0.134\%}{E}\right)^2 + (0.234\%)^2} \tag{5.16}$$

On the basis of this result, it was possible to consider the GEANT resolution of the forward endcap. It finally enables the possibility to run a simulation similar to the procedure for the barrel. The desired experimentally obtained smearing is preset in the digitisation and the GEANT resolution is quadratically subtracted to receive the smearing which has to be added onto the hits. Another full simulation with the setup used for the forward endcap leads to the following response curve shown in fig. 5.25.

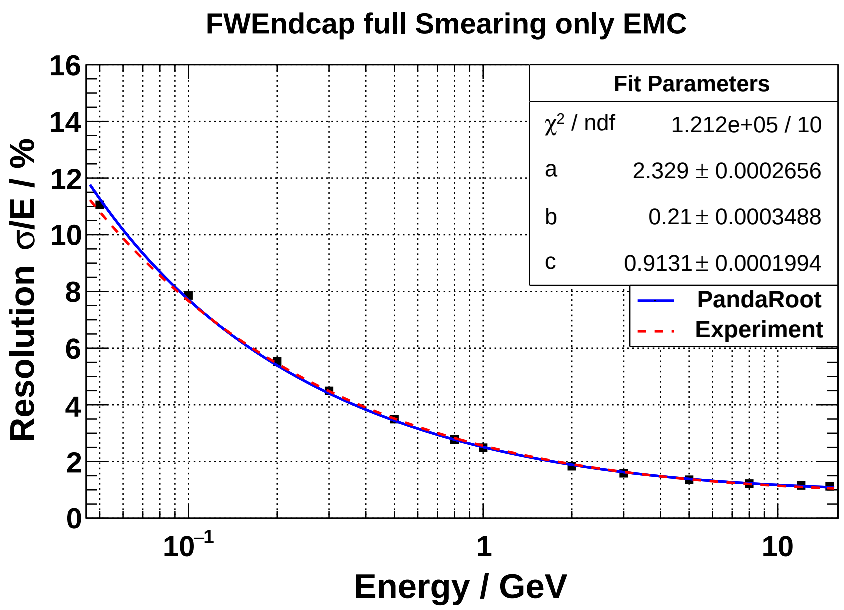

Figure 5.25: Response curve of the PandaRoot forward endcap EMC with the ideal digitisation path compared to the experimental data. To visualise the alignment the graph is scaled logarithmically.

As the graph shows, the two response functions match with only very slight deviations in the low energy range. This shows that the pre-smearing method has worked out very well and the generated GEANT resolution can be used for the forward endcap. As a first conclusion, the path of the ideal digitisation turned out promising results after adjusting it to the experimental values.

Chapter 6

Discussion and Outlook

Within the scope of this work the response of the electromagnetic calorimeter model of the future $\overline{\text{P}}$ANDA detector was investigated in the PandaRoot framework. It was optimised in regard to the experimental deduced response function. Examining the PandaRoot response for the two main components of the electromagnetic target calorimeter, the barrel and the forward endcap, turned out to produce a wide variety of outcomes. First of all the calculation of the resolution itself could be figured out and corrected, but, furthermore, many bugs and flaws of the existing PandaRoot code were observed. These will also be subject of discussion in this chapter.

6.1 Progress and Achievements

The performed tests and considerations showed that the original PandaRoot simulation leads to wrong results concerning the energy resolution. The simulated resolution is constantly better than the response which was obtained from experiments with prototypes. This is shown in fig. 5.6 for the barrel compared to the PROTO120 results and in fig. 5.13 for the forward endcap and the corresponding prototype.

To approach this issue a further investigation revealed that the smearing of the simulated hits which has an influence on the resolution is performed in the digitisation. As shown in the PandaRoot data flow in fig. 4.2 the digitisation divides into two paths. The ideal and real digitisation. The default way of digitising the hits in PandaRoot is the *real digitisation*. It uses many coefficients which are preset in the parameter database to rebuild the full read-out chain from the crystals to the SADC on a strict theoretical basis. Furthermore, the simulation assumes perfectly calibrated crystals so no possible calibration errors are taken into account which would be represented by the constant term of the response function. Since the resulting response was not matching the experiment, an approach with the parameters adjusted to their reasonable limits was started, but with no sufficient result. These reasons demonstrate the demand to adapt the digitisation.

An approach with a transition to a more experiment-like digitisation was started. Therefore, the less complex *ideal digitisation* was reprogrammed and adjusted to the experimental values. To align the response curve with the experimental energy resolution several steps had to be performed. First, the intrinsic GEANT resolution was examined by running a full simulation with no smearing in the digitisation. The different energy resolution values calculated by the Novo-Fit were afterwards fitted with the response function discussed in section 3.4. With this result the next step was to implement the desired experimental smearing in the digitisation and quadratically subtract the obtained GEANT resolution to receive the smearing which ultimately has to be added in the digitisation. Using this technique, the resulting resolution is defined by the user simply through the three coefficients of the response function.

This worked out very well for the barrel, however, when determining the simulated intrinsic resolution of the forward endcap the resulting plots could not be fitted due to the unusual shape shown in fig. 5.19. This issue has its origin in the full energy deposition in one crystal. One indication is the affected multiplicity. In contrast to the barrel EMC the forward endcap has nearly cuboid instead of tapered crystals which means there is no non-linear light collection. Its implementation at the barrel EMC is before the digitisation and responsible for a pre-smearing of the energy values. However, this is not the case at the forward endcap. If a lower energetic photon hits the EMC and deposits its full energy in one crystal, with no smearing in the digitisation, a delta-like peak could be observed. At higher energies more crystals are involved which leads to the observed wider distribution. To solve this issue a basic pre-smearing was implemented by hand to re-engineer the GEANT resolution. This approach leads to a response function for the forward endcap GEANT simulation which was then used in the digitisation. Finally, this altered way of digitising the hits results in a remarkable agreement of experimental and simulated resolution which is shown in fig. 6.1. All the displayed data points are taken into account for the fit, however, ROOT version 6.12/06 produces a display error at the edge of the plot. The simulated response function only shows slight discrepancies with the experimentally obtained resolution. These might be aroused by the Novo-Fits for each data point where the resulting resolution has, apart from the calculated error, also an error dependant on the fitting parameters entered by the user which can be estimated around $\pm 1\%$ as described in section 5.1.1. Furthermore, the fits through the data points to obtain the GEANT resolution are a possible cause of deviations.

Since the energy resolution is now adapted and tightly linked to the experimental results this leaves the question of the accuracy of these results over the whole energy range. The PROTO120 from which the most recent values derive consists of 120 crystals of geometry type 1,2 and 3. Compared to the 11,360 crystals, in geometries from type 1 to type 11, the whole barrel will consist of, this is a rather small sample although the beam hit the centre of the prototype and not all crystals are affected by a hit. [9] Furthermore, the experiments performed at the MAMI facility with the PROTO120 only reached up to 744 MeV [25]. This means that any higher values of the experimental energy resolution were extrapolated from the obtained formula.

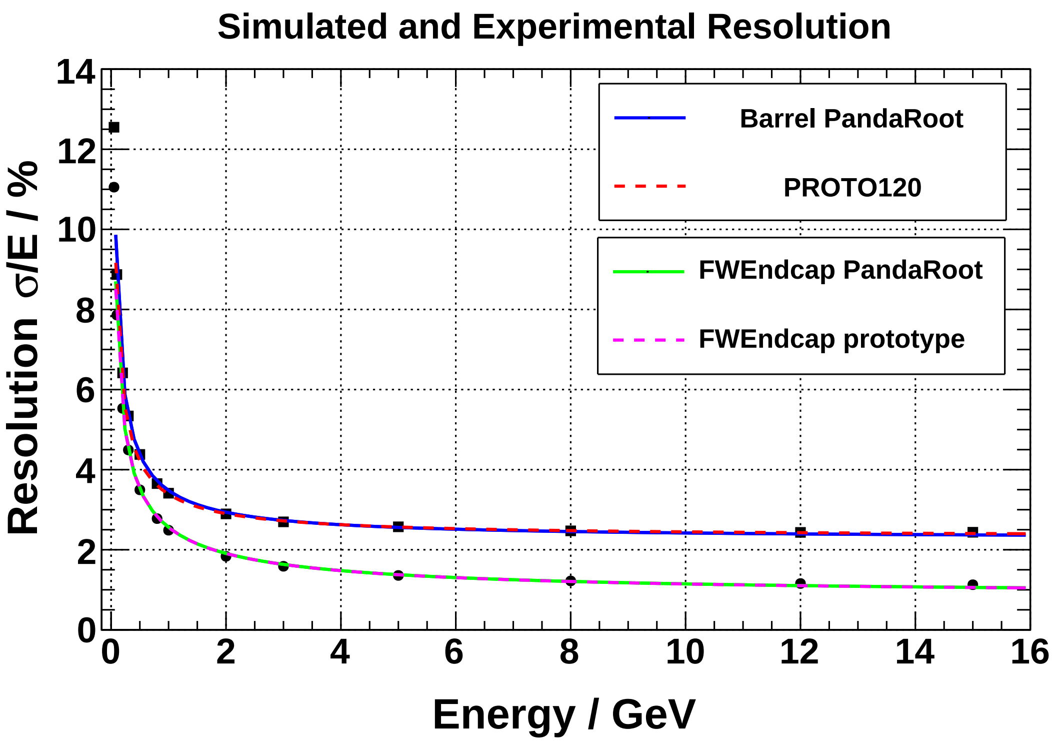

Figure 6.1: Response curves obtained with the improved PandaRoot ideal digitisation compared to the experimental prototype tests. The squares and dots are obtained data points from PandaRoot simulations.

Since the referred data of the prototypes for the barrel and the forward endcap several further developments have been done or are still ongoing, which could affect the energy resolution. While re-coding the digitisation these considerations were taken into account. It is now possible to change the three decisive values of the energy resolution formula in the general parameter file *all.par* found in *~/fairsoft_may18/pandaroot/macro/params/*. These were added at the end of the digitisation parameters for the respective $\overline{\text{P}}$ANDA EMC component and the current values for the barrel are shown in table 6.1.

name	symbol	name in file	current value
stochastic term	a	StochasticTerm_a	0.0246
noise term	b	NoiseTerm_b	0.0016
constant term	c	ConstantTerm_c	0.0232

Table 6.1: Barrel energy resolution terms in *all.par* with their current value displayed.

The generally adjusted energy resolution provides an improvement of the PandaRoot data analysis, since the algorithms can now operate with the same resolution as it would occur in an experiment. The experimental approach of the ideal digitisation which combines the steps from *PndEmcHitsToWaveform* and *PndEmcWaveformToDigi* to *PndEmcMakeDigi* does not only provide a more precise resolution. This shortcut also makes the digitisation faster and the general code more transparent and clear, which results in an easier understanding of the procedure for further possible edits in the future. The only disadvantage of the ideal digitisation is that it is not suitable for time-based simulations. These need the waveforms simulated in the real digitisation in order to include pile-ups for example.

As a conclusion the investigation revealed that the real digitisation path is flawed and needs to be adjusted at least in terms of the energy resolution, but also concerning other issues discussed in the outlook. As an alternative way of digitising based on the experiment but also as a reference for a future time-based capable model the ideal digitisation path can be used.

6.2 Outlook

As discussed in the last section, the resolution of PandaRoot was adjusted according to the prototype tests. However, these prototypes only represent a small portion of the detector and there was also only a single simulated hit position in the middle of the prototype. Although this position enables the best comparison to the experimental data, it has to be noted that the barrel is composed of different crystal geometries. These also have an influence on the behaviour of the detector. Strong pyramidal truncated crystals focus the light better on the APD. This should result in a better resolution at low energies and a worse resolution at high energies compared to the rectangular crystals. Due to its pure crystal dependant nature, such behaviour should be reproduced by the existing correct geometry and non linear light collection in the code of PandaRoot. Consequently as a next step for the future an investigation of different θ angles and the corresponding resolution could be started. So far there has been only one more prototype PROTO60, composed of type-6 crystals, in existance. Unfortunately it was the first prototype for the $\overline{\text{P}}$ANDA EMC and, therefore, used outdated electronics. Nevertheless, for high energies the effect of the altered electronics should be negligible. This enables the comparison of its response to a simulation with high energies in the corresponding barrel region.
Furthermore, since most of the tests were performed with only the EMC being simulated a next step could be to run several simulations with the full detector. In this case two things are of particular interest. First, the differences between those two simulations can be investigated, but also a comparison with experimental data where obstacles were put in front of the beam can be performed.

During the investigation of the PandaRoot response many other issues of the code were observed. When simulating 10 GeV photons hitting the barrel exactly at the position where the other tests were performed a weird pattern emerges in the energy spectrum. This effect is visualised in fig. 6.2. Exactly at the 10 GeV edge the accumulating peak jumps up about 100 counts which is reversed at an energy of 10.05 GeV so that the resulting peak is not continuous. Both plots show the same energy range, however, the right peak is much wider which results from the performed energy resolution correction. This is a good visualisation that the default resolution was constantly too good. Interestingly this discontinuity does not occur in the ideal digitisation which leaves the conclusion that it has to be an issue within the real digitisation. An investigation could be started about what causes this behaviour in the more complex real digitisation.

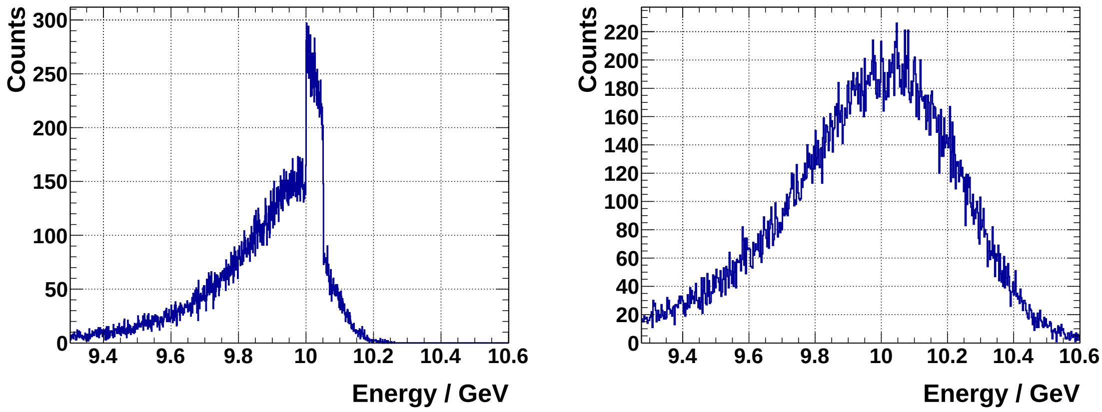

(a) real digitisation (default)

(b) ideal digitisation

Figure 6.2: Resulting histograms for simulated 10 GeV photons digitised with both options.

Another issue concerning the energy reconstruction is the peak position. In general when the calorimeter is hit with photons of a specific energy one would expect a peak which accumulates right before this energy value. Due to the conservation of energy the right edge of the peak would be on the exact energy value of the impinging photon since no higher energy than the initial one can be reconstructed. This is exactly what was observed when determining the forward endcap GEANT resolution at higher energies.
However, the resulting peak when running a full simulation typically exceeds the theoretical boundary of the initial energy. This is due to an implemented energy correction which shifts the whole distribution according to a preset factor. This is why the resolution should not be affected by this shift, although the absolute position of the peak is. The aim of this correction is to align the peak position with the energy of the impinging particle to enable a sufficient reconstruction of the energy.

Nevertheless, during the simulations it has been noticed that the peak position does not match the energy of the initial photons emitted by the particle gun. Moreover, it also differs for both tested components. While the accumulating peak at the barrel is almost always at a higher than the actual energy, the corresponding peak for the forward endcap is typically too low. Two exemplary plots visualising this phenomenon are shown in fig. 6.3. The accumulated data in the histogram was fitted with the Novosibirsk function where the statistics show the calculated peak which is marked in red. A reason for this behaviour at the barrel might be the non linearity light collection implemented before the digitisation and a missing or wrong calibration correction afterwards.

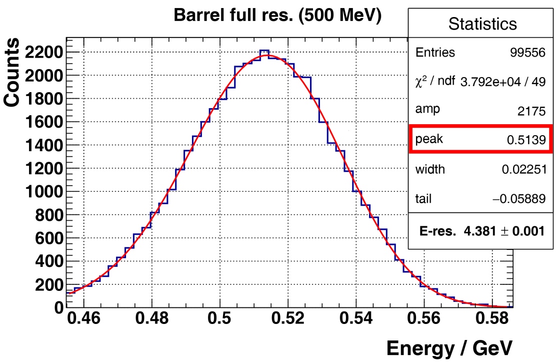

(a) Barrel (b) Forward endcap

Figure 6.3: Exemplary plots visualising the peak position of the barrel and forward endcap reconstruction.

At this point further investigations were started with π^0 mesons decaying into two photons. The simulation was set up using the particle gun to shoot pions with a kinetic energy of 800 MeV into the barrel respectively the forward endcap. This energy was chosen since both produced photons will most likely end up in the forward endcap when shooting in the forward direction. However, they usually hit close to the elliptical hole so a slightly decreased energy could be used at further tests. A visualisation of the desired hit positions of this simulation is shown in fig. 6.4 while the reconstructed energy is displayed in fig 6.5.

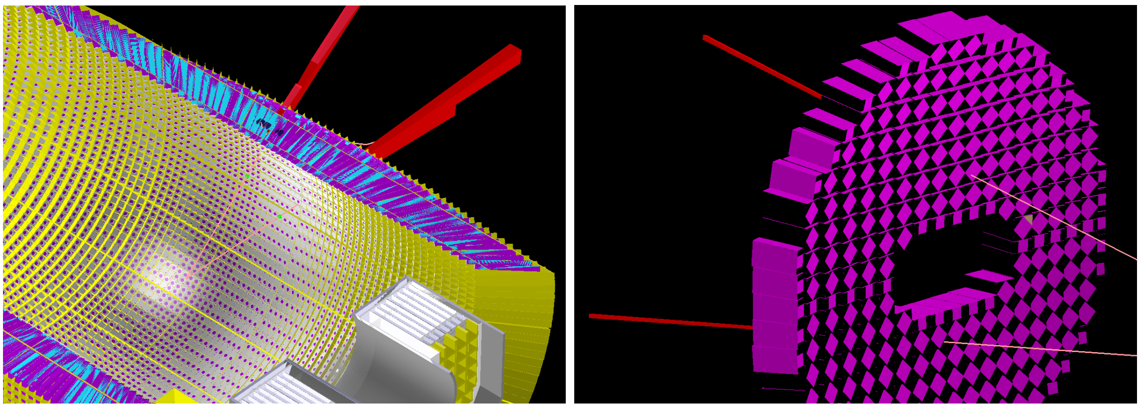

(a) Barrel (b) Forward endcap

Figure 6.4: Simulated π^0 mesons decaying into two photons which hit the barrel and the forward endcap.

The shapes of the peaks look marginally different which has to do with the difference in counts and therefore the amplitude. The amplitude at the barrel is much higher. Due to the setup of the performed test it is more likely that both photons hit the barrel than both hitting the forward endcap. Since for the forward endcap many events occurred where photons hit other parts of the EMC or sometimes the side of the inner most forward endcap crystal the reconstruction result is worse. For example when photons hit near the middle opening a shower leakage can occur due to the missing crystals. Another factor is the transition region between the barrel and the forward endcap. Both components are treated as independent detectors in the readout so if the shower spreads on both parts it will not be combined.

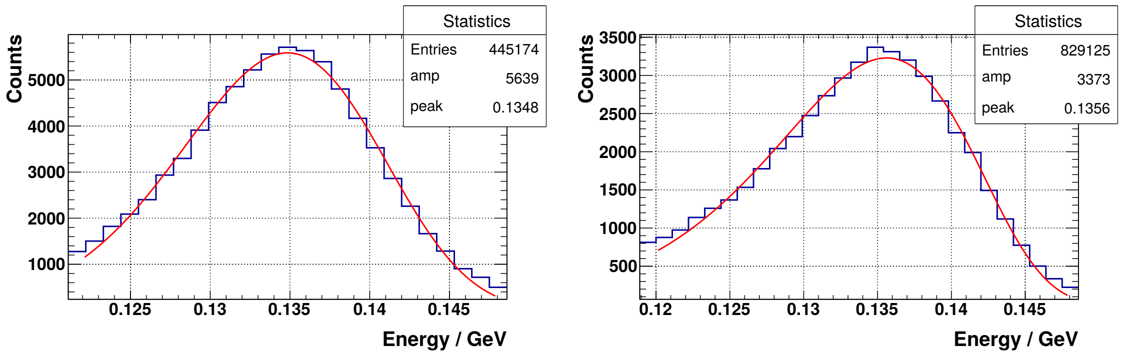

(a) Barrel

(b) Forward endcap

Figure 6.5: Reconstructed invariant mass for the simulated π^0 mesons decaying into two photons fot the two components.

Interestingly the results show that a reconstruction of the initial pion energy by combining the γ's produced almost the same initial pion invariant mass at both components. So to conclude, although the peaks for equal energetic photons hitting the EMC have a different position at the forward endcap and the barrel, the resulting reconstruction of the invariant mass is still not affected by this. Since only a few rudimentary test concerning this topic were performed, a further investigation could be beneficial such that the opening angle of the two gammas is not the leading part in the reconstruction of the invariant mass of a π^0.

During the simulations a low energetic peak in the photon spectrum has been observed frequently. This peak is an accumulation of low energetic photons at the beginning of the spectrum with energies approximately between 3 MeV and 10 MeV. Fig. 6.6 exemplifies this phenomena for a simulation of the whole detector when shooting 50 MeV photons into the barrel without any smearing in the digitisation.

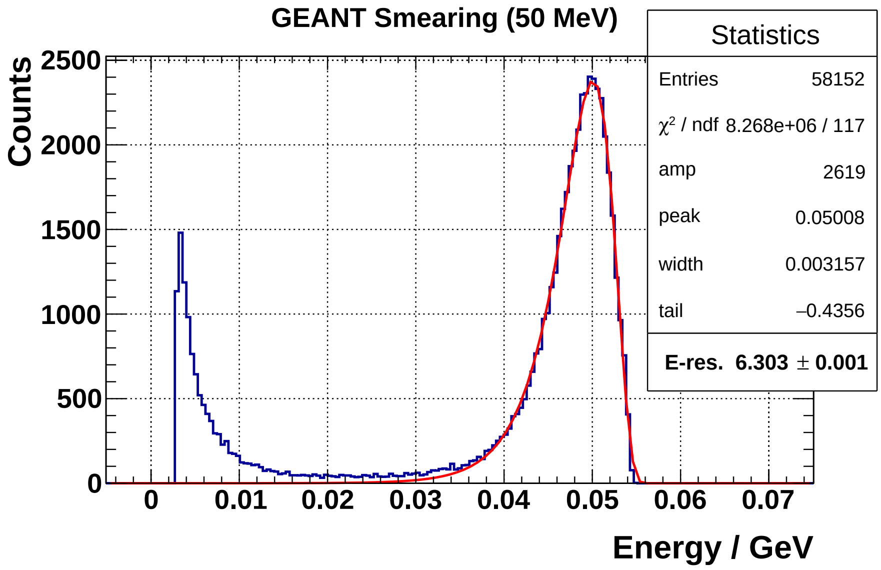

Figure 6.6: Exemplary energy spectrum to visualise the observed low energetic peak right above the threshold when simulating the full $\overline{\text{P}}$ANDA detector.

This peak could have several reasons. For instance, one of the electrons produced in pair production could escape, which leads to an incorrect measurement of the energy. This has already been observed in prototype tests where the effect occurred particularly with dead material in front of the detector. Furthermore it depends on the amount of crystals used for the reconstruction so the bigger the matrix the smaller the low energetic peak. Experimental tests with the prototype PROTO60 and a GEANT simulation are shwon in fig. 6.7. This means that the other parts of the detector might already influence the photons before the shower process (pre-showering) or in the case of simulating only the EMC backscattering out of the hit crystals could occur. This might be a hint that the reconstruction or the aggregation of the hits to one bump or respectively the separation of those (so called "bump splitting") does not work correctly. If the bumps are split to sharp electrons originating from the same incident photon can be assigned to different bumps. This is currently being optimised to improve the assignment of the low energetic photons to the peak. An analysis of the detected position of these entries can be the first step, followed by a detailed comparison between the plots respectively the line shapes of the whole detector and only the EMC simulation.

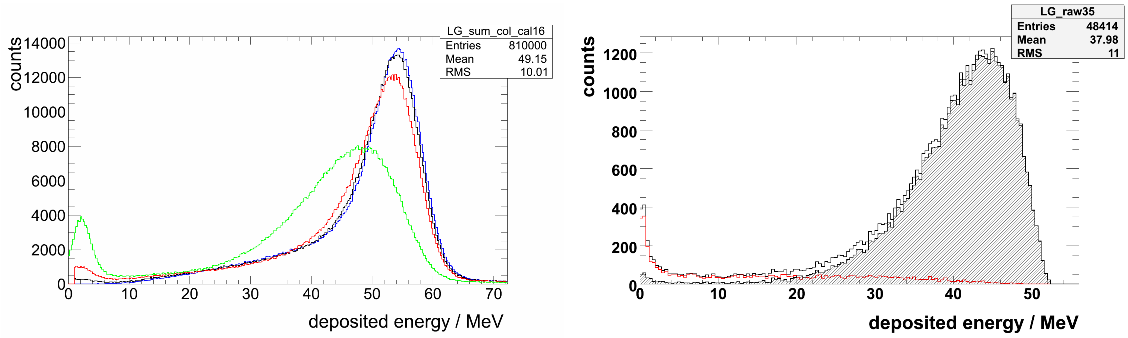

(a) experimental measurements

(b) GEANT simulation

Figure 6.7: Low energetic peak from experiments and simulations with 52.32 MeV photons hitting the prototype PROTO60. [29] The left histogram shows the line shapes resulting from the experimental matrix with DIRC and TOF dummies in front. The energy sum over the full PROTO60 is plotted in blue, the sum over the inner 25 crystals in black, the sum over the inner 9 crystals in red and the central crystal in green. The right histogram shows a GEANT simulation of the experiment with a DIRC sample in front. The energy deposition in the central crystal is plotted. The red curve represents the deposited energy when conversion in the DIRC occurred, the black curve with the shaded area when no pair production occurred and the black curve all events.

As a conclusion of this work, the resolution of the simulated $\overline{\text{P}}$ANDA detector EMC is now aligned with experimental data and can furthermore be easily changed. An altered way of digitisation was established and is seen as an alternative to the default digitisation which is currently being reworked. However, several flaws of which some could be resolved were observed. These will ultimately lead to further investigations.

Appendix

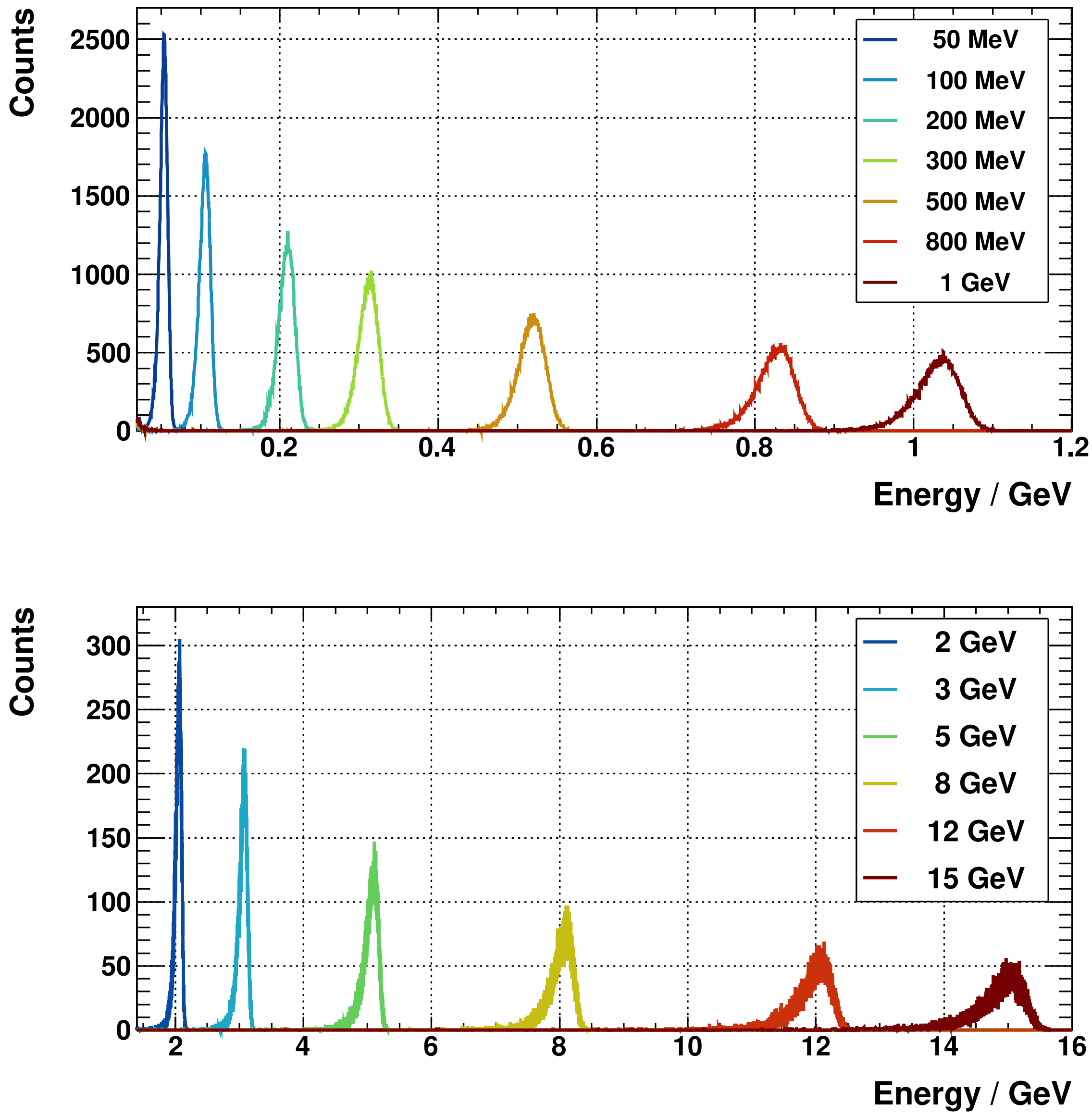

Figure 6.8: Line-shapes for the simulated energies with the default PandaRoot setup. The spectrum was split into two plots for a better visualisation.

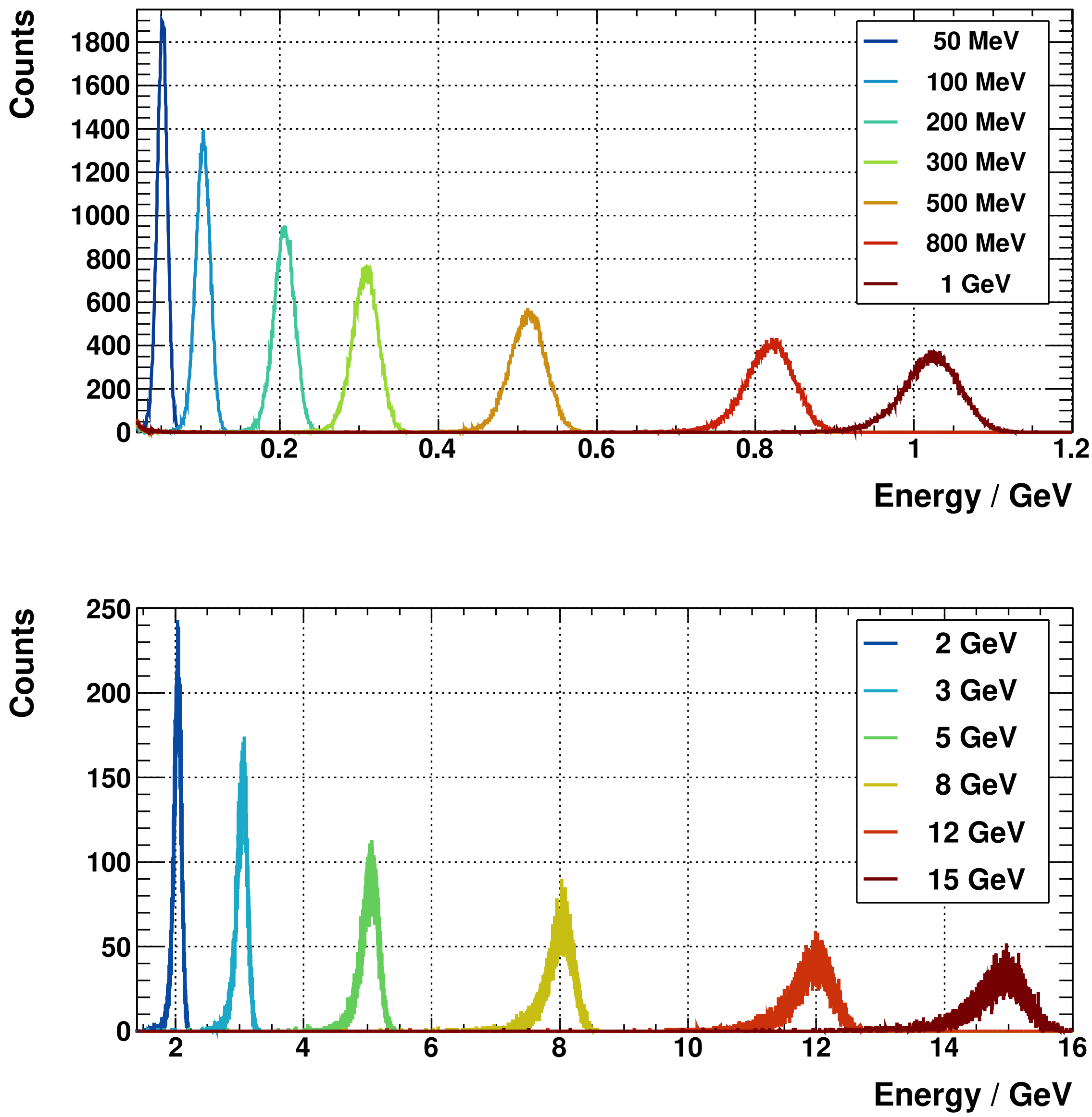

Figure 6.9: Line-shapes for the simulated energies using the adjusted ideal digitisation path. The spectrum was split into two plots for a better visualisation.

List of Figures

List of Tables

List of Acronyms

APD Avalanche Photo Diode

APFEL ASIC for PANDA Front-end Electronics

APPA Atomic, Plasma Physics and Applications

ASIC Application Specific Integrated Circuit

ATLAS A Toroidal LHC ApparatuS

CERN European Center for Nuclear and Particle Research
(Conseil européen pour la recherche nucléaire)

CBM Compressed Baryonic Matter

EMC Electromagnetic Calorimeter

FAIR Facility for Antiproton and Ion Research

FWHM Full Width at Half Maximum

GEANT Geometry and Tracking

GSI Gesellschaft für Schwerionenforschung

HESR High Energy Storage Ring

LAAPD Large Area Avalanche Photo Diode

MAMI Mainzer Mikrotron

MVD Micro Vertex Detector

NUSTAR Nuclear Structure Astrophysics and Reactions

PANDA Antiproton Annihilation at Darmstadt

PID Particle Identification

PMT Photomultiplier Tube

PWO-II lead tungstate ($PbWO_4$) second generation

UNILAC Universal Linear Accelerator

Bibliography

[1] Scott Aaronson. *Quantum Computing since Democritus*. Cambridge University Press, 2013.

[2] Christian Rudolph. *Search for the Standard Model Higgs boson in the dimuon decay channel with the ATLAS detector*. Technische Universität Dresden, Dissertation, 2014.

[3] Facility for Antiproton and Ion Research: The particle accelerator facility of FAIR and GSI. `https://www.gsi.de/en/researchaccelerators/fair.htm`. Accessed: Apr. 2019.

[4] Barry R. Holstein John F. Donoghue, Eugene Golowich. *Dynamics of the Standard Model*. Cambridge University Press, 2014.

[5] A. O. Sushkov, W. J. Kim, D. A. R. Dalvit, and S. K. Lamoreaux. New experimental limits on non-newtonian forces in the micrometer range. *Phys. Rev. Lett.*, 107, 2011.

[6] The Standard Model of Particle Physics. `https://www.azoquantum.com/Article.aspx?ArticleID=14`. Accessed: May 2019.

[7] Gesellschaft für Schwerionenforschung: FAIR and GSI brochures. `https://www.gsi.de/en/press/fair_and_gsi_brochures.htm`. Accessed: May 2019.

[8] V. Schaa P. Schütt R. Bär, U. Krause. The new fair accelerator complex at gsi: Project, controls challenges and first steps. Accessed: May 2019.

[9] Werner Erni et al. Technical Design Report for $\overline{\text{P}}$ANDA Electromagnetic Calorimeter (EMC). 2008.

[10] Malte Albrecht. The forward endcap of the electromagnetic calorimeter for the PANDA detector at FAIR. *Journal of Physics: Conference Series*, 2015.

[11] Christian W. Fabjan and Fabiola Gianotti. Calorimetry for particle physics. *Rev. Mod. Phys.*, 75:1243–1286, 2003.

[12] P. Klenze T. Le Bleis. Physics simulation with GEANT4. 2014.

[13] Vanet Souza, G Medina-Tanco, and Jeferson A. Ortiz. Fluorescence photons produced in air by extensive air showers. 10 2004.

[14] Prof. Robin D. Erbacher. Measuring particles' energy through Electromagnetic and Hadron interactions - Presentation. https://www.slideserve.com/liam/calorimetry-energy-measurements. Accessed: July 2019.

[15] Vitreous State Laboratory of the catholic state University of America: Photomultiplier tubes. `http://www.vsl.cua.edu/cua_phy/index.php/MainPage:Nuclear:Summer2013:FastAmplifier`. Accessed: May 2019.

[16] D.J.A.Cockerill R.M. Brown. Nuclear Instruments and Methods in Physics Research: Electromagnetic calorimetry. 2012.

[17] Markus Moritz. PID with the Panda EMC. Presentation at PID workshop GSI Darmstadt. 2018.

[18] Avalanche photodiodes. `https://www.perkinelmer.com/CMSResources/Images/44-6538APP_AvalanchePhotodiodesUsersGuide.pdf`. Accessed: June 2019.

[19] Fergus Wilson Adrian Bevan. Afit user guide. 2010.

[20] Markus Moritz. *Ansprechverhalten des PROTO 60, Untereinheit des PANDA Detektors, auf hochenergetische Photonen*. University of Giessen, Germany, 2009. Diplomthesis.

[21] Rene Brun and Fons Rademakers. Root — an object oriented data analysis framework. *Nuclear Instruments and Methods in Physics Research Section A: Accelerators, Spectrometers, Detectors and Associated Equipment*, 389(1):81 – 86, 1997. New Computing Techniques in Physics Research V.

[22] Stefano Spataro and the PANDA Collaboration. *The PandaRoot framework for simulation, reconstruction and analysis*. Journal of Physics: Conference Series **331** 032031, 2011.

[23] Facility for Antiproton and Ion Research: FairRoot. `http://cbmroot.gsi.de/`. Accessed: Apr. 2019.

[24] Stefano Spataro and the PANDA Collaboration. *Event Reconstruction in the PandaRoot framework*. Journal of Physics: Conference Series **396** 022048, 2012.

[25] Christoph Rosenbaum. *Optimization of the Front-End electronics of the PANDA Barrel EMC*. University of Giessen, Germany, Dissertation, 2016.

[26] HAMAMATSU. Si APD type no. S11048 Specification Sheet. 2018.

[27] PerkinElmer. Avalanche photodiodes: A user's guide. 2018.

[28] Wayne Lippert. *Konzepte der Kalibration eines Prototypsdes EM-Kalorimeters für $\overline{\mathrm{P}}$ANDA*. University of Giessen, Germany, 2010. Bachelor-Thesis.

[29] Markus Moritz. Measurements and improvements of the response of the $\overline{\mathrm{P}}$ANDA-EMC prototype PROTO 60 to high energetic particles and photons in accelerator experiments, 2013. Dissertation.

Danksagung

An dieser Stelle möchte ich mich zunächst bei meiner Familie, ganz besonders bei meinen Eltern, bedanken, die mir das Studieren ermöglichen und mich seit jeher unterstützen. Ohne Euren Rückhalt wäre ich sicherlich nicht da, wo ich jetzt bin.
Ein herzliches Dankeschön möchte ich außerdem an Herrn Prof. Kai-Thomas Brinkmann und die Arbeitsgruppe Brinkmann richten, dich mich sehr warm empfangen und direkt als Mitglied der Gruppe aufgenommen hat. Insbesondere richtet sich meinen Dank hier an Dr. Markus Moritz, der meine Arbeit betreut hat und mich bei Fragen und Problemen aller Art tatkräftig unterstützt hat, aber auch an Dr. Hans-Georg Zaunick, der immer für Fragen offen war und gerne im Bacheloranten Büro vorbei kam und Motivation verbreitet hat. Weiterer Dank gilt hier auch für die Begleitung beim Schreibprozess, das Korrekturlesen meiner Arbeit und die Unterstützung bei Formalitäten. An dieser Stelle möchte ich mich auch bei Mrs. Rebecca Kingdom-Herrmann bedanken für ein weiteres Korrekturlesen dieser Arbeit.
Ein sehr großer Dank geht auch an meine Kommilitonen Sven, Kim und Yannik im Büro, die mir mit Rat und Tat zur Seite standen, aber auch stets für eine angenehme Arbeitsatmosphäre und lustige Stimmung gesorgt haben. Dadurch ging das Forschen und anschließende Schreiben der Arbeit einfach leichter von der Hand. Des Weiteren möchte ich mich bei Jonny und Jan bedanken, die mir stets zur Seite standen bei der Bewältigung der großen Mengen an Plots.
Zuletzt gilt mein Dank meinen Freunden, die mich während des Bachelorstudiums immer begleitet, motiviert und unterhalten haben.

Selbstständigkeitserklärung

Hiermit versichere ich, die vorgelegte Thesis selbstständig und ohne unerlaubte fremde Hilfe und nur mit den Hilfen angefertigt zu haben, die ich in der Thesis angegeben habe. Alle Textstellen, die wörtlich oder sinngemäß aus veröffentlichten Schriften entnommen sind, und alle Angaben die auf mündlichen Auskünften beruhen, sind als solche kenntlich gemacht. Bei den von mir durchgeführten und in der Thesis erwähnten Untersuchungen habe ich die Grundsätze guter wissenschaftlicher Praxis, wie sie in der ‚Satzung der Justus-Liebig-Universität zur Sicherung guter wissenschaftlicher Praxis' niedergelegt sind, eingehalten. Gemäß § 25 Abs. 6 der Allgemeinen Bestimmungen für modularisierte Studiengänge dulde ich eine Überprüfung der Thesis mittels Anti-Plagiatssoftware.

....	....
Ort, Datum	Unterschrift